Chemical Science

ROYAL SOCIETY OF CHEMISTRY

REVIEW

View Article Online
View Journal | View Issue

Open Access Article. Published on 19 janvris 2024. Downloaded on 23.02.2025 18:44:43.
This article is licensed under a Creative Commons Attribution-NonCommercial 3.0 Unported Licence.

Check for updates

Cite this: *Chem. Sci.*, 2024, **15**, 2323

# Molecular modulation strategies for two-dimensional transition metal dichalcogenide-based high-performance electrodes for metal-ion batteries

Mingyuan Gu,[a] Apparao M. Rao,[b] Jiang Zhou [c] and Bingan Lu *[a]

Received 30th October 2023
Accepted 2nd January 2024

DOI: 10.1039/d3sc05768b

rsc.li/chemical-science

In the past few decades, great efforts have been made to develop advanced transition metal dichalcogenide (TMD) materials as metal-ion battery electrodes. However, due to existing conversion reactions, they still suffer from structural aggregation and restacking, unsatisfactory cycling reversibility, and limited ion storage dynamics during electrochemical cycling. To address these issues, extensive research has focused on molecular modulation strategies to optimize the physical and chemical properties of TMDs, including phase engineering, defect engineering, interlayer spacing expansion, heteroatom doping, alloy engineering, and bond modulation. A timely summary of these strategies can help deepen the understanding of their basic mechanisms and serve as a reference for future research. This review provides a comprehensive summary of recent advances in molecular modulation strategies for TMDs. A series of challenges and opportunities in the research field are also outlined. The basic mechanisms of different modulation strategies and their specific influences on the electrochemical performance of TMDs are highlighted.

## 1. Introduction

The enormous energy demand in modern society is causing excessive consumption of non-renewable energy sources and serious environment pollution. Energy resources, such as wind and solar energy, are clean and renewable, which are highly desirable for the long-term sustainable development of modern society. The main problem associated with these renewable clean energy sources is their intermittent characteristics, making energy storage systems (ESSs) necessary to store such intermittent energy for later use as a continuous and stable power. Due to their inherent advantages of low cost, long life-span, and high efficiency, secondary batteries are one of the ideal candidates for storing energy.[1] After decades of development, lithium-ion batteries (LIBs) have been successfully

[a]*School of Physics and Electronics, Hunan University, Changsha, P. R. China. E-mail: luba2012@hnu.edu.cn*
[b]*Department of Physics and Astronomy, Clemson Nanomaterials Institute, Clemson University, Clemson, SC 29634, USA*
[c]*School of Materials Science and Engineering, Central South University, Changsha, 410083, P. R. China*

**Mingyuan Gu**

*Mingyuan Gu received his bachelor's degree in electronic science and technology from Hunan University in 2012. His research interests include the design and preparation of advanced electrolytes and electrode materials for potassium ion batteries.*

**Bingan Lu**

*Bingan Lu, professor of Hunan University, obtained his PhD in physics from Lanzhou University in 2012. He has extensive experience in aqueous electrolyte batteries, potassium ion batteries and zinc ion batteries. He has published over 250 papers in many prestigious journals, including Nature, National Science Review, Nature Sustainability, and Nature Communications, with an H-index of 83 and other-citation of ∼20 000. He also is a Clarivate Highly Cited Researcher.*

© 2024 The Author(s). Published by the Royal Society of Chemistry 

Open Access Article. Published on 19 janvris 2024. Downloaded on 23.02.2025 18:44:43. This article is licensed under a Creative Commons Attribution-NonCommercial 3.0 Unported Licence.

commercialized and are ubiquitous in our daily lives. However, the low abundance of lithium resources may restrict large-scale LIB-based ESSs.[2,3] Therefore, alternate secondary metal-ion batteries with higher earth-abundance of the corresponding metals, such as sodium ion batteries (NIBs),[4–6] potassium ion batteries (PIBs),[7–10] and zinc ion batteries (ZIBs),[11–13] have been extensively studied. Among various battery systems, electrode materials play an important role in the battery's electrochemical performance. Therefore, developing advanced electrode materials is desired for low cost, long lifespan, high efficiency, and large scale secondary electrochemical ESSs.

Normally with a formula of $MX_2$ (M is composed of transition metals in group 4 to group 7, and X = S, Se, Te), 2D transition metal dichalcogenides (TMDs) have attracted much attention in the field of energy storage due to their 2D structure and tunable physical and chemical properties.[14–16] In monolayer $MX_2$, X atoms are distributed in the outer layers, while the M atoms that form covalent bonds with X atoms are sandwiched between the two outer layers of X atoms. The adjacent $MX_2$ layers in TMDs are coupled by weak van der Waals (vdW) forces, and the interlayers allow the intercalation of metal ions. For example, Whittingham demonstrated that $Li^+$ can be inserted and extracted reversibly in the interlayer of $TiS_2$ at a high speed in his pioneering work.[17] In addition, the large interlayer spacing of $MoS_2$ (0.62 nm) theoretically makes it easy to accommodate metal ions, such as alkali metal ions ($Li^+$, $Na^+$, and $K^+$), $Zn^{2+}$, *etc.*[18–20] Furthermore, the conversion reaction of some TMDs in the deep discharge state provides them with a high theoretical specific capacity. However, structural aggregation, restacking, and limited cycling stability originating from the conversion reaction during cycling still exist.[21,22] These negative factors cause TMD electrode materials to exhibit unsatisfactory electrochemical performance in metal ion batteries.

To address these issues, a large amount of research has been conducted to tune and optimize the properties of TMDs. Different morphologies of TMDs,[23–25] such as nanoflowers,[26] nanorods,[27] *etc.*, were explored to increase the specific surface area and relieve the structural stress during cycling. The TMDs' larger specific surface area can increase the contact area with the electrolytes, which is beneficial for faster ion diffusion and better rate performance. The lower structural stress is beneficial for maintaining structural integrity and improving long-term cycling stability. Coupling with carbon materials is also one of the commonly used strategies, which can not only reduce the charge transfer impendence, but also alleviate the structural aggregation caused by vdW interaction.[28–30] The above strategies effectively enhance TMDs' electrochemical performance, but they all modify TMDs from an 'external' perspective, and the basic properties of TMDs remain unchanged. In contrast, molecular modulation strategies modify the TMD molecules from an 'internal' perspective. Molecular modulation is mainly carried out at the molecular or atomic level, through the purposeful modulation of specific parts or regions of TMD molecules, so as to realize the effective modulation of TMDs' properties. Table 1 summarizes the cycling performance of some TMDs before and after molecular modulation, showing the advantages of molecular modulation.[31–58] As a result, molecular modulation strategies are of great significance for the development of TMDs.

In this review, we will introduce and summarize various molecular modulation strategies for TMD electrodes used in metal ion batteries, including phase engineering, defect engineering, interlayer spacing expansion, heteroatom doping, alloy engineering, and bond modulation. We begin by introducing the basic properties of different TMDs. Next, we focus on the mechanisms of different modulation methods and their specific influences on the TMDs' properties for metal-ion storage. Lastly, the challenges and perspectives of TMDs as metal-ion battery electrodes are outlined. We expect that this review will help improve the overall understanding of various molecular modulation mechanisms for TMDs in the application of electrochemical storage and serve as an excellent reference for the future development of TMD-based electrodes.

## 2. Basic properties of TMDs

### 2.1 Crystal structure

Due to the different coordination and stacking sequences of transition metals, TMDs exhibit polymorphs and stacking polytypes. For monolayer TMDs, two typical coordination structures exist for metal atoms: trigonal prismatic and octahedral coordination.[59] As shown in Fig. 1a, the trigonal prismatic coordination can be expanded to hexagonal symmetry (belongs to the $O_h$ (or $D_{3h}$) point group) with Bernal stacking (AbA) (the upper and lower case letters represent chalcogen and metal atoms, respectively) in the monolayer, namely, the 1H phase.[60] The octahedral coordination can be expanded to tetragonal symmetry (belongs to the $D_{3d}$ point group) with rhombohedral stacking (AbC), namely, the 1T phase (Fig. 1b). Due to distortions, other phases can also be found, such as the 1T′ phase (Fig. 1c). As shown in Fig. 1d–f, for bulk TMDs, the three most common polymorphs are 1T, 2H, and 3R, where the letters represent trigonal, hexagonal, and rhombohedral symmetry, and the digits indicate the number of $MX_2$ units in the unit cell (in other words, the number of $MX_2$ layers in the stacking sequences).[61,62] Among them, 2H and 3R phases can both be formed by stacking the 1H phase in different ways with a stacking sequence of AbA BaB and AbA BcB CaC, respectively.[63] A single TMD can also exist in the form of various polymorphs or stacking polytypes, depending on its synthesis method. For example, natural $MoS_2$ usually exhibits the 2H phase. However, 1T or 3R phases are often found in synthesized $MoS_2$.[64,65] Among the above several phases, 1T and 2H have been widely studied in metal ion batteries.

### 2.2 Electronic structure

The electrical properties of TMDs depend on the transition metals' coordination environment and their d orbital filling states.[62] In both 1H and 1T phases, the non-bonding d bands of TMDs are located within the gap between the bonding and antibonding bands of M–X bonds. Due to the influence of the lattice field, the d orbitals of transition metals with trigonal prismatic coordination ($O_h$) split into three groups, $d_{z^2}(a_1)$,

Table 1 Summary of TMDs' cycling performance before and after molecular modulation

| Materials | Cycling performance | Current density | Systems | Ref. |
|---|---|---|---|---|
| **Phase engineering** | | | | |
| 2H-$MoS_2$ | 16.4 mA h $g^{-1}$ after 300 cycles | 1 A $g^{-1}$ | LIBs | 31 |
| 2H-$MoS_2$/C | 350 mA h $g^{-1}$ after 300 cycles | | | |
| 1T-$MoS_2$/C | 870 mA h $g^{-1}$ after 300 cycles | | | |
| 2H-$MoS_2$@PNC | 369.9 mA h $g^{-1}$ after 250 cycles | 0.5 A $g^{-1}$ | NIBs | 32 |
| 1T/2H-$MoS_2$@NC | 389.5 mA h $g^{-1}$ after 250 cycles | | | |
| 1T/2H-$MoS_2$@PNC | 472.6 mA h $g^{-1}$ after 250 cycles | | | |
| $MoS_2$-0 T | 182 mA h $g^{-1}$ after 280 cycles | 1 A $g^{-1}$ | NIBs | 33 |
| $MoS_2$-9 T | 310 mA h $g^{-1}$ after 280 cycles | | | |
| 2H-$MoS_2$ | 100 mA h $g^{-1}$ after 50 cycles | 0.1 A $g^{-1}$ | NIBs | 34 |
| 1T-$MoS_2$ | 410 mA h $g^{-1}$ after 150 cycles | | | |
| 2H-$MoS_2$NFs | 308 mA h $g^{-1}$ after 50 cycles and 63.6 mA h $g^{-1}$ after 415 cycles | 0.1 A $g^{-1}$, 1 A $g^{-1}$ | NIBs | 35 |
| $TiO_2$–2H-$MoS_2$NFs | 593 mA h $g^{-1}$ after 50 cycles and 341 mA h $g^{-1}$ after 700 cycles | | | |
| TiO–1T-$MoS_2$NFs | 676 mA h $g^{-1}$ after 50 cycles and 501 mA h $g^{-1}$ after 700 cycles | | | |
| CNT@2H-$MoS_2$ | 254.6 mA h $g^{-1}$ after 50 cycles | 0.1 A $g^{-1}$ | NIBs | 36 |
| 1T-$MoS_2$ | 89.7 mA h $g^{-1}$ after 50 cycles | | | |
| CNT@1T-$MoS_2$ | 542.3 mA h $g^{-1}$ after 50 cycles | | | |
| 2H-$MoSe_2$ | ~20 mA h $g^{-1}$ after 50 cycles | 0.1 A $g^{-1}$ | ZIBs | 37 |
| 1T-$MoSe_2$ | 138.8 mA h $g^{-1}$ after 50 cycles | | | |
| 1T-$MoSe_2$/CC | 265.1 mA h $g^{-1}$ after 50 cycles | | | |
| **Defect engineering** | | | | |
| $MoS_2$ | 170 mA h $g^{-1}$ after 220 cycles | 0.1 A $g^{-1}$ | LIBs | 38 |
| $MoS_2$/C-CPM | 831 mA h $g^{-1}$ after 220 cycles | 0.2 A $g^{-1}$ | | |
| $WS_2$–SPAN-1 | 278 mA h $g^{-1}$ after 450 cycles, 292 mA h $g^{-1}$ after 1400 cycles | 0.5 A $g^{-1}$, 2 A $g^{-1}$ | NIBs | 39 |
| $WS_2$–SPAN-2 | 464 mA h $g^{-1}$ after 450 cycles, 354 mA h $g^{-1}$ after 1400 cycles | | | |
| $WS_2$–SPAN-3 | 246 mA h $g^{-1}$ after 450 cycles and 206 mA h $g^{-1}$ after 1400 cycles | | | |
| $MoS_2$ | 45 mA h $g^{-1}$ after 100 cycles | 0.5 A $g^{-1}$ | NIBs | 40 |
| BD-$MoS_2$ | 354 mA h $g^{-1}$ after 100 cycles | | | |
| NC@$MoS_2$ | 103 mA h $g^{-1}$ after 100 cycles | 0.1 A $g^{-1}$ | NIBs | 41 |
| NC@$MoS_2$–Ar | 430 mA h $g^{-1}$ after 100 cycles | | | |
| NC@$MoS_2$–VS | 495 mA h $g^{-1}$ after 100 cycles | | | |
| $VSe_2$ | 264 mA h $g^{-1}$ after 100 cycles and 79 mA h $g^{-1}$ after 500 cycles | 0.5 A $g^{-1}$, 3 A $g^{-1}$ | PIBs | 42 |
| P–$VSe_{2-x}$ | 351 mA h $g^{-1}$ after 100 cycles and 143 mA h $g^{-1}$ after 1000 cycles | | | |
| Commercial $WS_2$ | 85.6 mA h $g^{-1}$ after 50 cycles, — | 0.1 A $g^{-1}$, 2 A $g^{-1}$ | PIBs | 43 |
| P–$WS_2$ | 173.7 mA h $g^{-1}$ after 50 cycles and 25.6 mA h $g^{-1}$ after 50 cycles | | | |
| Sv–$WS_2$ | 230.8 mA h $g^{-1}$ after 50 cycles and 93.2 mA h $g^{-1}$ after 200 cycles | | | |
| $MoS_2$ 750 | ~5 mA h $g^{-1}$ | 1 A $g^{-1}$ | ZIBs | 44 |
| $MoS_{2-x}$ 250 | 88.6 mA h $g^{-1}$ after 1000 cycles | | | |
| $VSe_2$-SS | 75.8 mA h $g^{-1}$ after 1800 cycles | 4 A $g^{-1}$ | ZIBs | 45 |
| $VSe_{2-x}$-SS | 175.8 mA h $g^{-1}$ after 1800 cycles | | | |
| **Interlayer spacing expansion** | | | | |
| $MoS_2$ | 248 mA h $g^{-1}$ after 100 cycles | 0.2 A $g^{-1}$ | LIBs | 46 |
| $MoS_2$@PANI | 701 mA h $g^{-1}$ after 100 cycles | | | |
| $MoS_2$/PANI | 1207 mA h $g^{-1}$ after 100 cycles | | | |
| $MoS_2$ | ~90 mA h $g^{-1}$ after 100 cycles | 0.3 A $g^{-1}$ | NIBs | |
| $MoS_2$@PANI | ~150 mA h $g^{-1}$ after 100 cycles | | | |
| $MoS_2$/PANI | 456 mA h $g^{-1}$ after 100 cycles | | | |
| c-$WSe_2$ | 61 mA h $g^{-1}$ after 150 cycles | 0.1 A $g^{-1}$ | PIBs | 47 |
| WSNC | 384 mA h $g^{-1}$ after 200 cycles | | | |
| ns-$MoS_2$ | ~200 mA h $g^{-1}$ after 100 cycles | 0.5 A $g^{-1}$ | PIBs | 48 |
| exp-$MoS_2$ | ~360 mA h $g^{-1}$ after 100 cycles | | | |
| p-$MoS_2$ | 11.9 mA h $g^{-1}$ after 1000 cycles | 1 A $g^{-1}$ | ZIBs | 49 |
| $MoS_2$/PANI-150 | 91.6 mA h $g^{-1}$ after 1000 cycles | | | |
| **Heteroatom doping** | | | | |
| Bulk $WSe_2$ | 69 mA h $g^{-1}$ after 50 cycles, — | 0.1 A $g^{-1}$, 1 A $g^{-1}$ | NIBs | 50 |
| 2H-$WSe_2$–2 | 281 mA h $g^{-1}$ after 50 cycles and 158 mA h $g^{-1}$ after 900 cycles | | | |
| 2H-$WSe_2$–1 | 321 mA h $g^{-1}$ after 50 cycles and 202 mA h $g^{-1}$ after 900 cycles | | | |
| 1T-$WSe_2$–Sn | 460 mA h $g^{-1}$ after 50 cycles and 285 mA h $g^{-1}$ after 900 cycles | | | |
| OMSCF-500 | 60 mA h $g^{-1}$ after 100 cycles and 21 mA h $g^{-1}$ after 100 cycles | 0.1 A $g^{-1}$, 1 A $g^{-1}$ | NIBs | 51 |
| OMSCF-300 | 221 mA h $g^{-1}$ after 100 cycles and 79 mA h $g^{-1}$ after 100 cycles | | | |

Open Access Article. Published on 19 janvris 2024. Downloaded on 23.02.2025 18:44:43.
This article is licensed under a Creative Commons Attribution-NonCommercial 3.0 Unported Licence.

© 2024 The Author(s). Published by the Royal Society of Chemistry 

Open Access Article. Published on 19 janvris 2024. Downloaded on 23.02.2025 18:44:43. This article is licensed under a Creative Commons Attribution-NonCommercial 3.0 Unported Licence.

Table 1 (Contd.)

| Materials | Cycling performance | Current density | Systems | Ref. |
|---|---|---|---|---|
| MSCF | 232 mA h $g^{-1}$ after 100 cycles and 87 mA h $g^{-1}$ after 100 cycles | | | |
| OMSCF-400 | 330 mA h $g^{-1}$ after 100 cycles and 181 mA h $g^{-1}$ after 100 cycles | | | |
| Pristine $MoS_2$ | ~47 mA h $g^{-1}$ after 50 cycles | 1 A $g^{-1}$ | ZIBs | 52 |
| D-$MoS_2$–O | 281.9 mA h $g^{-1}$ after 50 cycles | | | |
| **Alloy engineering** | | | | |
| $MoS_2$ | 228.9 mA h $g^{-1}$ after 400 cycles | 1 A $g^{-1}$ | LIBs | 53 |
| $Mo_{0.5}W_{0.5}S_2$ | 271.9 mA h $g^{-1}$ after 400 cycles | | | |
| $WS_2$ | 205.8 mA h $g^{-1}$ after 400 cycles | | | |
| $MoS_2$-NC | 385.63 mA h $g^{-1}$ after 1000 cycles | 0.2 A $g^{-1}$ | PIBs | 54 |
| $MoS_{1.5}Se_{0.5}$-NC | 531.56 mA h $g^{-1}$ after 1000 cycles | | | |
| $MoS_2$ | 18.3 mA h $g^{-1}$ after 1000 cycles | 2 A $g^{-1}$ | PIBs | 55 |
| $MoSe_2$ | 114.3 mA h $g^{-1}$ after 1000 cycles | | | |
| MoSSe | 220.5 mA h $g^{-1}$ after 1000 cycles | | | |
| $MoS_2$/rGO | 67.6 mA h $g^{-1}$ after 150 cycles | 0.1 A $g^{-1}$ | ZIBs | 56 |
| $MoSe_2$/rGO | 44.5 mA h $g^{-1}$ after 150 cycles | | | |
| MoSSe/rGO | 210.3 mA h $g^{-1}$ after 150 cycles | | | |
| **Bond modulation** | | | | |
| $MoSe_2$ | Almost no capacity after 20 cycles | 1 A $g^{-1}$ | LIBs | 57 |
| Red $MoSe_2$ | 1125.7 mA h $g^{-1}$ after 500 cycles | | | |
| MoSe–rGO | ~100 mA h $g^{-1}$ after 60 cycles | 0.1 A $g^{-1}$ | PIBs | 58 |
| $MoSe_{2+x}$–rGO | 168 mA h $g^{-1}$ after 300 cycles | | | |

$d_{x^2-y^2,xy}(e)$, and $d_{xz,yz}(e')$, with a sizeable gap (~1 eV) between the first two groups of orbitals. The d orbitals of transition metals with octahedral coordination ($D_{3d}$) split into two groups, $d_{z^2,x^2-y^2}(e_g)$ and $d_{yz,xz,xy}(t_{2g})$.[59] The filling states of non-bonding d bands play an important role in the electrical properties of TMDs. When the orbitals are fully occupied, such as in 2H-$MoS_2$ and 2H-$MoSe_2$,[66,67] the materials exhibit semiconducting behaviour. When the orbitals are partially filled, such as in $NbS_2$ and $VS_2$,[68,69] the materials show metallic behaviour. The phases and electrical properties of group 4–7 TMDs are summarized in Table 2.[59,61,63,70–76] In addition, although the chalcogen atoms have a smaller influence on the electronic properties of TMDs, the broadening of d bands and the corresponding decrease in bandgap with increasing chalcogen atom number can still be observed. For example, the bandgap of 2H-$MoS_2$, 2H-$MoSe_2$, and 2H-$MoTe_2$ decreases from 1.3 to 1.0 eV.[77]

The d electron counting of transition metals also plays a key role in selecting the preferred phase for TMDs. Group 4 TMDs with $d^0$ transition metal centers all possess an octahedral structure. While in group 5 TMDs ($d^1$), both the trigonal prismatic and octahedral structures exist. The trigonal prismatic phase accounts for the majority in group 6 TMDs ($d^2$), and

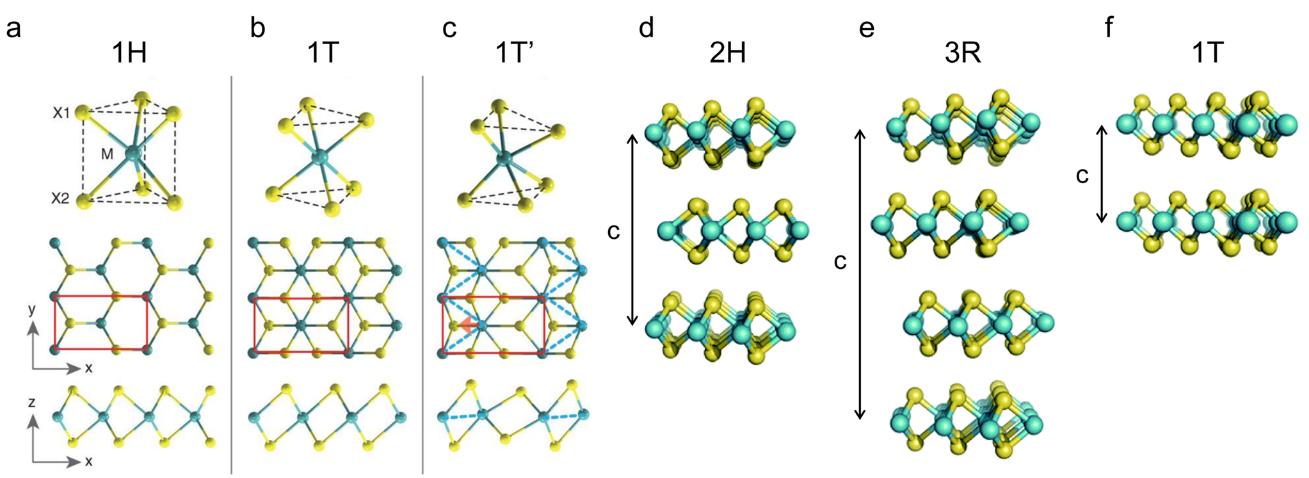


Fig. 1 Schematics of the polymorphs and stacking polytypes: (a–f) 1H, 1T, 1T′, 2H, 3R, and 1T. Reproduced with permission from (a–c) ref. 60. Copyright 2014, Science; (d–f) ref. 62. Copyright 2015, Royal Society of Chemistry.

 © 2024 The Author(s). Published by the Royal Society of Chemistry

Open Access Article. Published on 19 janvris 2024. Downloaded on 23.02.2025 18:44:43.
This article is licensed under a Creative Commons Attribution-NonCommercial 3.0 Unported Licence.

Table 2 Summary of phases and electrical properties of TMDs

| Group | Metal | Chalcogen | Phases | Electrical properties | Ref. |
|---|---|---|---|---|---|
| 4 | Ti | S | 1T | Semiconducting | 31 and 70 |
| | | Se | | | |
| | | Te | | | |
| 5 | V | S | 1T | Metal | |
| | | Se | | | |
| | | Te | | | 71 and 72 |
| 5 | Nb | S | 2H | Metal | 61 and 70 |
| | | Se | | | 70 and 73 |
| | | Te | 1T | | 61 and 70 |
| 6 | Mo | S | 2H | Semiconducting | 61 and 70 |
| | | Se | | | 70 and 73 |
| | | Te | | | 61 and 70 |
| 6 | W | S | 2H | Semiconducting | 61 and 70 |
| | | Se | | | 70 and 73 |
| | | Te | 1T′ | | 61 and 74 |
| 7 | Re | S | 1T′ | Semiconducting | 75 and 76 |
| | | Se | | | 61 and 63 |
| | | Te | — | — | — |

group 7 TMDs ($d^3$) mainly consist of a distorted octahedral phase.[59]

### 2.3 Metal-ion storage mechanisms

When TMDs serve as alkali metal-ion battery electrodes, reversible intercalation and extraction reactions occur first at a relatively high cutoff voltage (~1 V) with $A_xMX_2$ as the product (A represents alkali metal atoms).[78] The M–X bonding interactions are larger than the A–$MX_2$ interactions during these processes. When the discharge process continues, $TiX_2$ and $NbX_2$ still exhibit reversible intercalation and extraction processes due to the sufficiently strong M–X bonding. However, for the other TMDs whose M–X bonding interactions become smaller than the A–$MX_2$ interactions at a low voltage, a conversion reaction occurs with the products of M and $A_2X$. The reversibility of the conversion reactions is influenced by the dynamic properties of $MX_2$,[79] including the electrical properties, structural stability, and ion diffusion kinetics. The poor dynamic properties of $MX_2$ result in irreversible conversion reactions and the oxidation products of M and X in the first cycle. In the subsequent cycles, the redox couple changes into X/$A_2X$, which means that X replaces $MX_2$ as the active material. Due to their poor dynamic properties, the semiconducting phases $MoX_2$, $WX_2$, and $ReX_2$ exhibit irreversible conversion reactions.[80–82] In contrast, the excellent dynamic properties of $MX_2$ lead to reversible conversion reactions, where $MX_2$ can be reformed after an oxidation reaction. *i.e.*, $MX_2$ is always the active material. The metal phase $VX_2$ compounds have been demonstrated to exhibit partially reversible conversion reactions due to their better dynamic properties.[83–85] In addition, the voltage at which the conversion reaction begins usually varies depending on the materials and the intercalated alkali metal ions. For example, commercial 2H-$MoS_2$ begins to undergo a conversion reaction when discharged to 0.6 V in a LIB system. In NIB and PIB systems, however, the starting voltages decrease to 0.13 and 0.16 V, respectively.[86]

When TMDs are used in multivalent-ion batteries, no ion storage mechanism associated with the conversion reaction has been reported so far.[87] As a result, the main multivalent-ion storage mechanisms of TMDs are currently ion intercalation and extraction.

## 3. Molecular modulation strategies for TMDs in metal ion batteries

### 3.1 Phase engineering

The pristine electrical properties of different phases play a critical role in TMDs' electrochemical performance. For example, the conversion reaction is irreversible for the semiconducting phase Mo, W, and Re-based dichalcogenides due to their poor conductivities. Due to their much better conductivity, the conversion reaction becomes partially reversible in the case of metallic phase V-based dichalcogenides. As a result, converting semiconducting phase TMDs to the metallic phase could be an effective strategy to improve their electrical properties and electrochemical performance greatly. For example, Yao *et al.* prepared 1T-$MoS_2$@GO for a PIB anode.[88] As a comparison, 2H-$MoS_2$@GO was also prepared. Due to the much improved electronic conductivity, a partially reversible conversion reaction is achieved when using 1T-phase $MoS_2$, which is similar to the behaviour of metallic phase V-based dichalcogenides. In addition, 1T-$MoS_2$@GO exhibits a better electrochemical performance than 2H-$MoS_2$@GO at all the tested current densities. This section mainly discusses the phase engineering strategies of Mo and W-based dichalcogenides.

As shown in Fig. 2a and b, under a trigonal prismatic crystal field, the Mo 4d orbitals of $MoS_2$ are divided into $d_{xy,x^2-y^2}$, $d_{yz,xz}$, and $d_{z^2}$ groups, where $d_{z^2}$ is located at the lowest position of the orbitals.[89] Therefore, the two 4d electrons fill the $d_{z^2}$ orbital in pairs, making 2H-$MoS_2$ exhibit semiconducting behaviour. For 1T-$MoS_2$, the octahedral crystal field makes the Mo 4d orbitals split into $d_{xy,xz,yz}$ and $d_{z^2,x^2-y^2}$ groups. In this case, the two 4d electrons tend to parallelly occupy two of the three orbitals in the lower group following the minimum Coulomb energy principle, resulting in metallic behaviour. Therefore, manipulating the electronic structures of the Mo 4d orbitals is the key to transitioning from the semiconducting phase to the metallic phase for Mo-based dichalcogenides. The partial density of states (PDOS) of Mo 4d in different phases also confirms the above conclusion (Fig. 2c and d).[89]

In addition to the greatly improved electrical conductivity, the 1T phase usually shows a larger interlayer spacing than the 2H phase, resulting in faster ion diffusion rates and smaller volume changes during cycling.[90,91] Bai *et al.* prepared the 1T-$MoS_2$/C composite for $Li^+$ storage. The prepared 1T-$MoS_2$ not only exhibits metallic conductivity but also shows an expanded interlayer spacing of 0.94 nm (Fig. 2e).[31] The enlarged interlayer space of 1T-$MoS_2$ compared to that of 2H-$MoS_2$ (0.62 nm, Fig. 2f) enables rapid intercalation and extraction of $Li^+$ and buffers the volume changes, leading to improved electrochemical performance. The 1T-$WS_2$ nanoflowers (NFs) with an enlarged interlayer spacing of 0.67 nm (0.62 nm for 2H-$WS_2$)

Open Access Article. Published on 19 janvris 2024. Downloaded on 23.02.2025 18:44:43.
This article is licensed under a Creative Commons Attribution-NonCommercial 3.0 Unported Licence.

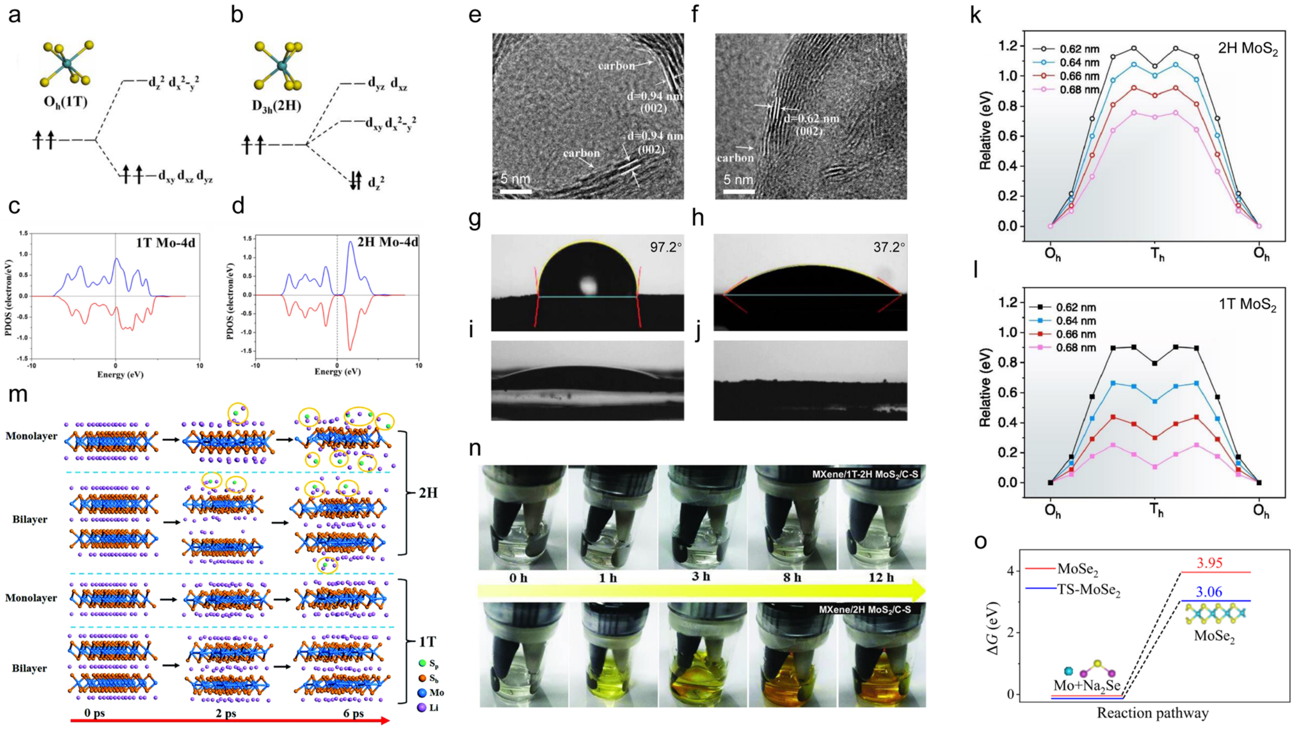

Fig. 2 Electronic structure manipulation of the Mo 4d orbitals as a key to transition from a semiconducting to a metallic phase for Mo-based dichalcogenides. (a and b) The occupation of electrons in Mo 4d orbitals under the crystal fields of the 1T phase and 2H phase. Calculated PDOSs of 4d states of Mo for the (c) 1T phase and (d) 2H phase. HRTEM images of the (e) 1T-$MoS_2$/C hybrid and (f) 2H-$MoS_2$/C hybrid. Water contact angle measurements of (g) 3DG/2H-$MoS_2$ and (h) 3DG/1T-$MoS_2$. Electrolyte contact angle measurements of (i) 3DG/2H-$MoS_2$ and (j) 3DG/1T-$MoS_2$. Calculated energy profiles of $Zn^{2+}$ diffusion in (k) 2H phase and (l) 1T phase $MoS_2$ with different interlayer distances. (m) Snapshots of trajectories for lithiated 2H-$MoS_2$ monolayer, 2H-$MoS_2$ bilayer, 1T-$MoS_2$ monolayer, and 1T-$MoS_2$ bilayer nanosheets following 6 ps *ab initio* molecular dynamics (AIMD) simulations at 300 K. (n) Digital photos of glass vials with the MXene/1T–2H $MoS_2$–C–S and MXene/2H $MoS_2$–C–S batteries as discharge time increases (0.05C). (o) The Δ*G* values per formula unit of the reaction between $Na_2Se$/Mo and $MoSe_2$ under strained and unstrained conditions. Reproduced with permission from: (a–d) ref. 88. Copyright 2015, AIP Publishing; (e and f) ref. 31. Copyright 2019, Wiley-VCH; (g–j) ref. 96. Copyright 2019, Royal Society of Chemistry; (k and l) ref. 97. Copyright 2022, Elsevier; (m) ref. 102. Copyright 2016, Royal Society of Chemistry; (n) ref. 103. Copyright 2018, Wiley-VCH; (o) ref. 113. Copyright 2022, Springer Nature.

also exhibit better electrochemical performance than the 2H-$WS_2$ NFs and 2H-$WS_2$ sheets.[92]

When used as aqueous metal-ion battery electrodes, 1T-$MoS_2$ shows higher hydrophilicity than 2H-$MoS_2$, which is beneficial for wetting the electrolytes and increasing the ion diffusion rate.[93–95] The water contact angle measurements of three-dimensional graphene (3DG)/2H-$MoS_2$ and 3DG/1T-$MoS_2$ are shown in Fig. 2g and h.[96] 3DG/2H-$MoS_2$ shows a contact angle of 97.2°, which is much higher than 37.2° of 3DG/1T-$MoS_2$, suggesting that 1T-$MoS_2$ is highly hydrophilic. Liu *et al.* synthesized $MoS_2$ nanosheets with different 1T phase contents for aqueous zinc ion storage.[97,98] Because of the high conductivity and hydrophilicity of 1T-$MoS_2$, a tendency is observed that the electrochemical performance improves with increasing the content of the 1T phase, and the $MoS_2$ nanosheets with the highest content of the 1T phase exhibit the best electrochemical performance. The density functional theory (DFT) calculations showed that 1T-$MoS_2$ always exhibits lower $Zn^{2+}$ diffusion energy barriers than 2H-$MoS_2$ under the same interlayer spacing conditions (Fig. 2k and l).[97] In addition to its high hydrophilicity, 1T-$MoS_2$ also exhibits better organic electrolyte wettability (Fig. 2i) than 2H-$MoS_2$ (Fig. 2j).[96]

Moreover, during the conversion reaction process, taking $MoS_2$ as an example, the formation of polysulfides is unavoidable, resulting in the loss of active materials and the shuttle effect.[34,99] This phenomenon can be mitigated by converting 2H-$MoS_2$ to 1T-$MoS_2$ due to the latter's strong adsorption toward polysulfides and higher chemical stability.[100,101] As shown in Fig. 2m, the continuous release of S atoms from 2H-$MoS_2$ and the formation of polysulfides within 6 ps are evident for both monolayer and bilayer nanosheets from the AMID simulations.[102] In contrast, no S atoms are released from 1T-$MoS_2$ within 6 ps for both monolayer and bilayer nanosheets, demonstrating the higher chemical stability of 1T-$MoS_2$ compared to 2H-$MoS_2$. Furthermore, a polysulfide adsorption experiment was carried out under continuous discharge conditions (Fig. 2n).[103] For the MXene/1T–2H $MoS_2$–C–S nanohybrids, almost no change in the color of the electrolyte is observed during the 12 h discharging process. However, in the case of MXene/2H $MoS_2$–C–S nanohybrids, the color of the electrolyte changes from colorless to faint yellow within the first 3 h. Subsequently, the color of the electrolyte changes to dark yellow until the end of the discharge. Therefore, the strong adsorption of 1T-$MoS_2$ toward polysulfides enables it to have

 © 2024 The Author(s). Published by the Royal Society of Chemistry

Open Access Article. Published on 19 janvris 2024. Downloaded on 23.02.2025 18:44:43.
This article is licensed under a Creative Commons Attribution-NonCommercial 3.0 Unported Licence.

excellent cycling stability and behave as a promising S host. Zhang *et al.* prepared MXene/1T–2H $MoS_2$–C nanohybrids as an S host for Li–S batteries.[103] Compared to the MXene/2H $MoS_2$–C host, the MXene/1T–2H $MoS_2$–C–S electrode exhibits better cycling stability.

Phase engineering is a very effective strategy to improve the dynamic properties and electrochemical performance of Mo and W-based dichalcogenides, and many methods have demonstrated the successful preparation of their 1T phases.[104] The relatively lower temperature hydrothermal/solvothermal methods are often used to prepare 1T phase-containing Mo and W-based dichalcogenides.[105,106] When increasing the reaction temperature or annealing the 1T phase at a high temperature, the 2H phase can be obtained. For example, 1T-$MoS_2$ can be prepared by a hydrothermal reaction below 200 °C. When the reaction temperature is increased to 240 °C, only the 2H phase exists due to its higher thermodynamic stability.[88] More specifically, when performing hydrothermal/solvothermal reactions or other phase engineering strategies, foreign species intercalation,[107,108] vacancy and dopant introduction,[109,110] exfoliation-restacking,[111,112] *etc.*, are the main pathways for manipulating the Mo 4d electronic structures. Among these, foreign species (such as organic compounds) intercalation not only results in the formation of the 1T phase but can also regulate the Gibbs free energy of the redox reaction by using the strain. For example, Jiang *et al.* reported tensile-strained $MoSe_2$ (TS-$MoSe_2$) using 2-methylimidazole (2-MI) as a scaffold.[113] The introduction of 2-MI not only results in the formation of 1T-$MoSe_2$ but also reduces the Gibbs free energy of the redox chemistry (Fig. 2o), resulting in highly reversible sodium ion storage.

Since the 1T phase has many advantages, the phase transition ratio therefore becomes a very important parameter for the phase engineering strategy. From the viewpoint of thermodynamics, the 1T phase is metastable, and the 2H phase is more stable.[114] Therefore, it is hard to achieve a 100% phase transition for Mo and W-based dichalcogenides. Currently, most TMDs constructed by phase engineering strategies contain around 70% of the 1T phase (Table 3).[36,37,115,116] Although the electrochemical performance of these TMDs has been greatly improved, the construction of pure 1T phase Mo and W-based dichalcogenides is still desirable. He *et al.* reported that they induced a 100% phase transition of $MoS_2$ from the 2H phase to the 1T phase by electron-injection-engineering.[35] During the synthesis process, the reducing gases generated by the decomposition of melamine donate electrons to the $MoS_2$ precursor, triggering the formation of pure 1T phase $MoS_2$. Meanwhile, the TiO nanoparticles generated from the reduction of $TiO_2$ are chemically bonded with 1T-$MoS_2$, which ensures the stability of the 1T phase. In addition, a very interesting phenomenon was reported by Ding *et al.* where high magnetic fields can also induce the formation of pure 1T phase $MoS_2$ and $WS_2$.[33] They found that 1T-$MoS_2$ and 1T-$WS_2$ can be prepared by magneto-hydrothermal processing under magnetic fields of 8 T and 9 T, respectively.

In short, phase engineering can improve the electrical conductivity of Mo and W-based TMDs. Additionally, a larger interlayer spacing, better electrolyte wettability, and stronger polysulfide adsorption are also beneficial for rapid ion storage and stable cycling performance.

### 3.2 Defect engineering

Generally, ions insert into defect-free TMDs from the edges and diffuse along the interlayers.[117,118] The limited active sites and long diffusion paths are not beneficial for rapid ion storage, resulting in sluggish ion transport kinetics. Defects have been found to be able to increase the active adsorption sites, enhance the conductivity, improve the reactive kinetics, and create additional ion diffusion paths,[55,119–121] which can effectively alleviate the problems faced by defect-free TMDs.

According to the dimensions, the defects in TMDs can be divided into four main types: zero-dimensional (0D) point defects, one-dimensional (1D) line defects, two-dimensional (2D) planar defects, and three-dimensional (3D) volume defects.[122] Among them, the 0D point defects are more favorable due to their positive effects on the electrochemical performance and their easy and controllable incorporation.[123] Therefore, point defects will be mainly discussed in this section. For example, as shown in Fig. 3a–h,[124] the most commonly observed point defects in monolayer $MoS_2$ include the monosulfur

Table 3 Summary of the ratios of the 1T phase prepared by different phase engineering strategies

| Materials | Methods | 1T phase ratio (%) | Ref. |
|---|---|---|---|
| $MoS_2$ | Hydrothermal method: 160 °C for 24 h | 51 | 97 |
| $MoSe_2$ | Hydrothermal method: 200 °C for 12 h | 53.7 | 115 |
| $MoS_2$ | Hydrothermal method: 180 °C for 24 h + solvothermal method: 200 °C for 8 h | 60 | 116 |
| $MoSe_2$ | Solvothermal method: 220 °C for 24 h | 65 | 36 |
| $MoS_2$ | Solvothermal method: 200 °C for 12 h | 62.5 | 106 |
| $MoS_2$ | Solvothermal method: 180 °C for 20 h | 69.1 | 37 |
| $MoS_2$ | Exfoliated and restacked method | 70 | 93 |
| $MoS_2$ | Hydrothermal method: 160 °C for 24 h | 70 | 98 |
| $MoSe_2$ | Solvothermal method: 220 °C for 48 h | 78.6 | 90 |
| $MoSe_2$ | Plasma-assisted annealing method | 91 | 109 |
| $MoS_2$ | Solvothermal method: 210 °C for 24 h + annealing method:700 °C for 2 h | 100 | 35 |
| $MoS_2$ + $WS_2$ | Magneto-hydrothermal method | 100 | 33 |

Open Access Article. Published on 19 janvris 2024. Downloaded on 23.02.2025 18:44:43.
This article is licensed under a Creative Commons Attribution-NonCommercial 3.0 Unported Licence.

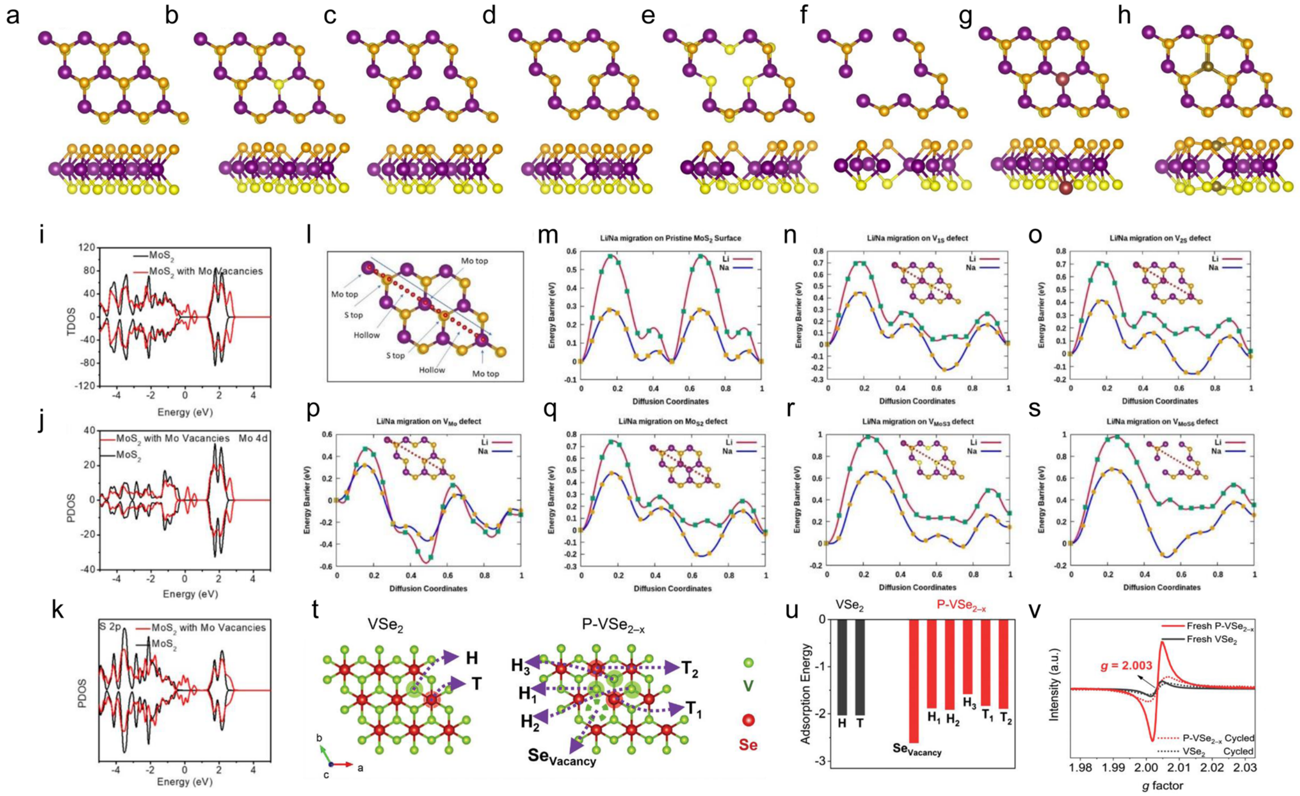


Fig. 3 Optimized geometry of various defects in monolayer $MoS_2$. (a) Pristine $MoS_2$, (b) $V_{1S}$, (c) $V_{2S}$, (d) $V_{Mo}$, (e) $V_{MoS3}$, (f) $V_{MoS6}$, (g) $Mo_{S2}$, and (h) $S2_{Mo}$ vacancies. The purple and yellow colored balls denote Mo and S atoms, respectively. The top layer of S atoms is in golden yellow color, and the bottom layers are in light yellow color. In the $Mo_{S2}$ vacancy, the maroon-colored ball represents the antisite Mo substituting a sulfur atom. In the $S2_{Mo}$ vacancy, the gray ball represents the antisite S substituting a Mo atom. The diffusion path for Li/Na on $MoS_2$ with defects. Total (i) and partial (j and k) charge density of states of $MoS_2$ with Mo vacancies and pristine $MoS_2$. Diffusion energy profiles for Li/Na diffusion barriers for (l) pristine $MoS_2$, (m) Li/Na migration path on pristine $MoS_2$, (n) monosulfur vacancy, (o) disulfur vacancy, (p) Mo vacancy, (q) $Mo_{S2}$ vacancy, (r) MoS3 vacancy, and (s) MoS6 vacancy. (t) $K^+$ adsorption sites on $VSe_2$ and P–$VSe_{2-x}$, and (u) their corresponding adsorption energies. (v) EPR spectra of $VSe_2$ and P–$VSe_{2-x}$ electrodes before and after one galvanostatic charge–discharge cycle. Reproduced with permission from (a–h and l–s) ref. 124. Copyright 2019, American Chemical Society; (i–k) ref. 126. Copyright 2019, American Chemical Society; (t–v) ref. 42. Copyright 2023, Wiley-VCH.

vacancy ($V_{1S}$), disulfur vacancy ($V_{2S}$), Mo vacancy ($V_{Mo}$), vacancy complex $V_{MoS3}$ ($V_{MoS6}$) of Mo and nearby three (six) sulfur, and two types of antisite defects where the Mo atom substitutes an S2 column ($Mo_{S2}$) or an S2 column substitutes a Mo atom ($S2_{Mo}$). The formation energies of various vacancies are listed in Table 2, from which it can be observed that the formation energies of $V_{1S}$, $V_{2S}$, and $V_{Mo}$ are lower than those of the other vacancies, implying that they are easier to form and are more widely studied.[122,123] In addition, it is worth pointing out that although the defect engineering strategies reported below claim that TMD electrodes containing anionic or cationic vacancies can be controllably synthesized, the preparation of TMD electrodes containing only specific types of defects has not yet been reported.

By manipulating the electronic structures of the Mo 4d orbitals, the conversion of Mo-based TMDs from a semi-conducting phase to a metallic phase was achieved *via* phase engineering, leading to a great improvement of conductivity and electrochemical performance. The presence of defects can also manipulate the electronic structures of the Mo 4d orbitals. Due to the presence of defects, the localized electrons generate midgap states within the valence or conduction bands, resulting in p-type or n-type conductors. The midgap states generate free charge carriers, thereby enhancing the conductivity.[125] As shown in Table 4, pristine $MoS_2$ exhibits a direct bandgap of around 1.67 eV. When different defects are created, the bandgap decreases to varying degrees, indicating enhanced conductivity. For example, Liang *et al.* reported nitrogen-doped carbon nanofiber@$MoS_2$ nanosheet arrays with sulfur vacancies for $Na^+$ storage.[41] The introduction of sulfur vacancies enhances the conductivity of the materials and serves as the new active site for adsorbing $Na^+$. Therefore, the charge transfer resistance is reduced, and the specific capacity and rate performance are improved. Li *et al.* developed a hollow microcube framework composed of ultrathin $MoS_2$ nanosheets rich in Mo vacancies.[126] Theoretical calculations reveal that the Mo vacancies can improve the electrical conductivity of $MoS_2$ due to the narrowed bandgap (Fig. 3i–k) and the enhanced interaction between $MoS_2$ and Na, resulting in rapid reaction kinetics and improved Na storage capacity.

 © 2024 The Author(s). Published by the Royal Society of Chemistry

Open Access Article. Published on 19 janvris 2024. Downloaded on 23.02.2025 18:44:43.
This article is licensed under a Creative Commons Attribution-NonCommercial 3.0 Unported Licence.

Table 4 The calculated vacancy formation energy (eV), energy gap (eV), adsorption energies ($E_{ad}$), and barrier heights (eV) of pristine and various types of defective $MoS_2$

| Vacancy | Vacancy formation energy (eV) | Energy gap $E_g$ (eV) | Adsorption energy for Li $E_{ad\text{-}Li}$ (eV) | Adsorption energy for Na $E_{ad\text{-}Na}$ (eV) | Barrier height for Li (eV) | Barrier height for Na (eV) |
|---|---|---|---|---|---|---|
| Pristine $MoS_2$ | — | 1.67 | −2.08 | −1.28 | 0.57 | 0.28 |
| $V_{1S}$ | 1.95 | 1.06 | −2.57 | −1.99 | 0.69 | 0.43 |
| $V_{2S}$ | 3.78 | 1.02 | −2.44 | −1.89 | 0.70 | 0.40 |
| $V_{Mo}$ | 5.73 | 0.09 | −3.92 | −1.81 | 0.46 | 0.32 |
| $V_{MoS3}$ | 7.90 | 0.64 | −2.83 | −2.09 | 0.91 | 0.65 |
| $V_{MoS6}$ | 13.89 | 0.03 | −3.37 | −2.28 | 0.95 | 0.67 |
| $MoS_2$ | 6.89 | 0.01 | −2.58 | −1.99 | 0.74 | 0.47 |
| $S2_{Mo}$ | 9.33 | 0.48 | −2.28 | −1.60 | — | — |

In addition, the presence of defects in TMDs is believed to be able to provide stronger binding sites for alkali metal atoms. The adsorption energies for Li and Na at the top site (above the top of a Mo atom) of pristine $MoS_2$ and at the seven defective regions are listed in Table 4.[124] It can be observed that pristine $MoS_2$ shows a Li adsorption energy of −2.08 eV and a Na adsorption energy of −1.28 eV. When different defects are created, the adsorption energies for Li and Na are higher than that of pristine $MoS_2$. The high adsorption energies of various defects indicate the easy binding and the favorable chemical interaction between Li/Na and defective $MoS_2$. Besides the adsorption energies, the diffusion kinetics are also important for the electrochemical reaction rate. As shown in Fig. 3l–s, the associated activation energy barriers of pristine $MoS_2$ and all types of defects were calculated with the fixed path.[124] For the pristine $MoS_2$ model, the path features two symmetrical absolute maxima, two symmetrical local maxima, and two local minima for the diffusion barriers when Li and Na pass through the two-unit cell (Fig. 3m). Consistent with the diffusion path of pristine $MoS_2$, only one maximum is found in the vicinity of the defects (Fig. 3n–s), as the barrier height disappears in the defect regions. Thus, it is clear that the presence of vacancies reduces the barrier height in the defective regions, and $Li^+$ and $Na^+$ can diffuse efficiently into the vacancy regions and then diffuse across the vacancies to the top site of the next cell in the $MoS_2$ plane (Fig. 3n–p). Although the introduction of vacancies enhances the barrier energies in the vicinity of the defects (Table 4), the barrier energies near 0.7 eV and 0.4 eV are believed to ensure the rate performance of LIBs and NIBs at room temperature. The enhanced adsorption energies of $V_{MoS3}$ and $V_{MoS6}$ essentially act as traps, which inhibits the atomic motion of $Li^+$ and $Na^+$ (Fig. 3r and s). The presence of antisite defects also promotes the migration of Li and Na atoms on the defective $MoS_2$ surface (Fig. 3q). However, in the case of antisite defect $S2_{Mo}$, the migration of both Li and Na ions ceases because the migrating $Li^+$ and $Na^+$ are repelled by the sulfur atoms replacing the Mo atoms. A systematic study is still lacking for the adsorption and diffusion properties of $K^+$ in pristine and defective $MoS_2$.

The presence of defects can enhance the conductivity and provide stronger and more binding sites, which is very beneficial for electrochemical performance. However, for those TMDs that undergo conversion reactions during cycling, the crystal structures experience a reconstruction process, which may be detrimental to the retention of defects. Sha *et al.* explored the role of anion vacancies of $VSe_2$ in $K^+$ storage.[42] They found that the existence of anion vacancies in $VSe_2$ can promote the electrochemical reaction kinetics. In addition, the defect regions provide more active sites (Fig. 3t), and they all exhibit large $K^+$ adsorption energies (Fig. 3u). However, the anion vacancies in $VSe_2$ are found to influence the first potassiation process primarily. In the subsequent cycles, they disappear and cannot be regenerated, which is demonstrated by electron paramagnetic resonance (EPR) (Fig. 3v). Although the vacancies in $VSe_2$ disappear after the first cycle, the electrochemical performance of defective $VSe_2$ is still much better than that of pristine $VSe_2$, which is interesting and needs further exploration. In the case of those TMDs that only undergo intercalation and extraction reactions, the defects may be preserved well during cycling. Liu *et al.* reported a $TiS_2$ anode rich in cation vacancies, which only experiences intercalation and extraction reactions during cycling.[127] *Ex situ* EPR spectra demonstrate that, even after 60 cycles, the EPR signal of defective $TiS_2$ is almost unchanged, indicating that the defects were well retained. Still, much work is needed to determine the clear relationship between the reaction types and defect retention.

It is believed that introducing defects will bring new ion diffusion pathways, thus enhancing the electrochemical reaction kinetics. An experiment designed by Zhang *et al.* demonstrated that small-size ions can also intercalate through the top surface of few-layer defective $MoS_2$ apart from the edges (Fig. 4a).[128] The color changes of $MoS_2$ flakes with sealed and open edges during cycling indicate that $Li^+$ can both intercalate through the top surface and the edges (Fig. 4b), and the process of intercalating through the top surface of $MoS_2$ flakes has much better reversibility. In the case of $Na^+$ storage (Fig. 4c and d), the $MoS_2$ flakes with sealed and open edges both exhibit excellent reversibility, although the ionic radius of $Na^+$ is higher than that of $Li^+$. This phenomenon is attributed to the relatively weak chemical binding between Na and $MoS_2$.[129] In contrast, no obvious change is observed when attempting to intercalate $K^+$ into sealed $MoS_2$, indicating that $K^+$ cannot intercalate through the top surface of defective $MoS_2$ flakes (Fig. 4e and f). The color changes of $K^+$ intercalated into $MoS_2$ flakes with open edges are similar to that of $Li^+$, indicating that the reversibility of this process is also poor. These observations demonstrate that the

Open Access Article. Published on 19 janvris 2024. Downloaded on 23.02.2025 18:44:43.
This article is licensed under a Creative Commons Attribution-NonCommercial 3.0 Unported Licence.

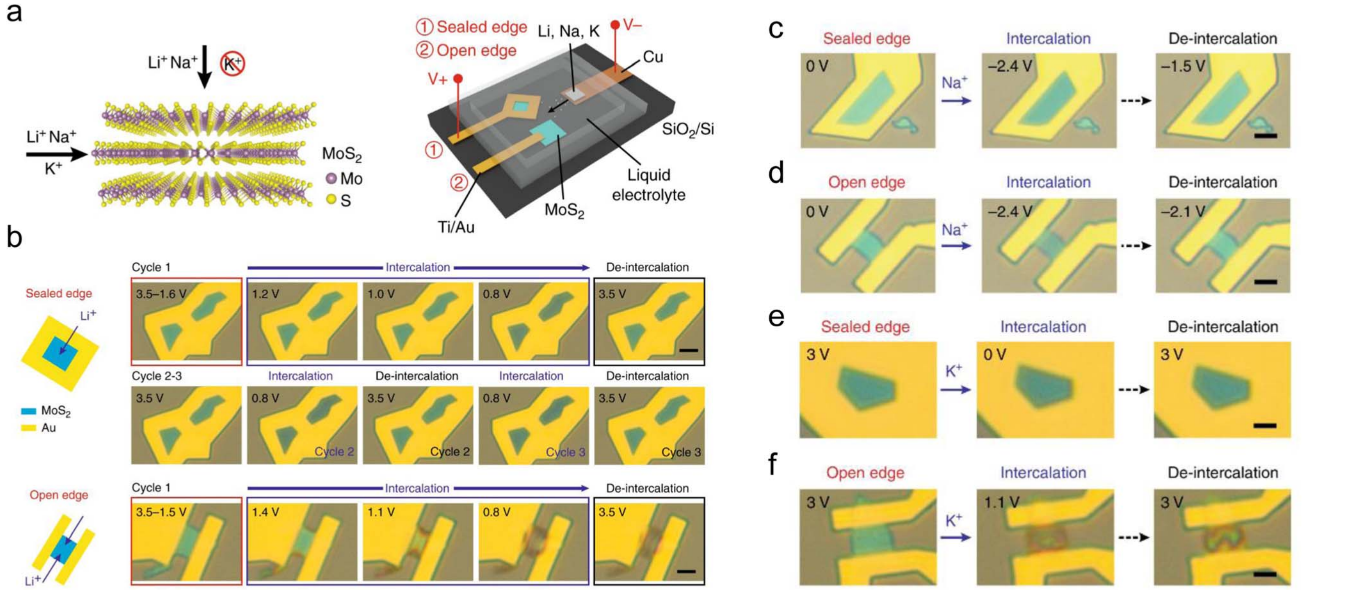


Fig. 4 Schematic representation of $MoS_2$ and of the experimental setup to study intercalation and de-intercalation. (a) $Li^+$, $Na^+$, and $K^+$ intercalation into $MoS_2$ through top and edge channels. An electrochemical cell is used to perform intercalation of $Li^+$, $Na^+$, and $K^+$ into $MoS_2$ with sealed and open edges. (b) *In situ* optical microscopy images of Li intercalation into $MoS_2$ through top surface and edges, respectively. Scale bars, 5 μm. (c and e) *In situ* optical microscopy images of Na and K intercalation into $MoS_2$ through the top surface. (d and f) *In situ* optical microscopy images of Na and K intercalation into $MoS_2$ through the edges. Scale bars in (c–f), 5 μm. Reproduced with permission from ref. 128. Copyright 2018, Springer Nature.

defects on the top surface of $MoS_2$ allow the intercalation of small-size ions (such as $Li^+$ and $Na^+$) but reject large-size ions (such as $K^+$). Similarly, additional 3D ion diffusion pathways have also been explored through theoretical or experimental studies.[40,42]

The large charge density of multivalent ions leads to a high ion intercalation and diffusion impedance in TMDs. Introducing defects can enhance the electrochemical reaction kinetics of TMDs, thus improving their storage capacity for multivalent ions. Xu *et al.* activated $MoS_2$ for $Zn^{2+}$ storage by introducing sulfur vacancies.[44] Compared to pristine $MoS_2$, $MoS_2$ with sulfur vacancies exhibits much greater capacity, better rate performance, as well as high capacity retention. Theoretical calculations reveal that the numerous defects act as the preferential intercalation sites for $Zn^{2+}$ storage. $MoS_2$ nanosheets with sulfur vacancies were also reported by Zhu *et al.* for $Mg^{2+}$ storage.[130] They showed that introducing defects into $MoS_2$ nanosheets improves the ability of $MoS_2$ to store $Mg^{2+}$. Bai *et al.* used defective $VSe_2$ for $Zn^{2+}$ storage by introducing selenium vacancies and reported an enhanced electrochemical performance.[45] By using theoretical calculations, they found that the presence of selenium vacancies adjusts the adsorption energy of $Zn^{2+}$, which makes the electrochemical reaction more reversible.

In short, introducing defects into TMDs can enhance their conductivity, provide more and stronger binding sites, create new ion transfer pathways, and shorten the diffusion paths of metal ions, which are beneficial for improving the ion storage capacity of TMDs. However, in some TMDs, the defects disappear after the first cycle and cannot be regenerated, yet electrochemical performance improvements can still be observed in the subsequent cycles. This phenomenon is interesting and has not been explained clearly yet. In addition, the clear relationship between the reaction types and defect retention also needs further studies for a better understanding.

### 3.3 Interlayer spacing expansion

A low ion diffusion barrier is essential for rapid ion transport in TMDs. Although the presence of defects has been demonstrated to accelerate ion diffusion, their positive effects only exist locally.[124] Therefore, a strategy that can comprehensively reduce the ion diffusion barriers of TMDs is needed. It has been reported that although the interlayer spacing of $ReS_2$ and $MoS_2$ is very similar (6.14 Å for $ReS_2$ and 6.15 Å for $MoS_2$), the diffusion barriers of $Li^+$ in $ReS_2$ nanosheets are significantly lower than that in $MoS_2$ nanosheets,[131] and the main reason is attributed to the much weaker vdW interactions between the adjacent layers in $ReS_2$ than that in $MoS_2$.[131,132] The weak vdW interactions between TMD interlayers are beneficial for rapid transport of ions with low impendence. As a result, weakening the vdW interactions between TMD interlayers could be an effective strategy to comprehensively reduce the ion diffusion barriers of TMDs. In addition to selecting some TMDs that exhibit weak vdW interactions on their own, such as $ReS_2$, a more effective and broadly applicable strategy is to expand the interlayer spacing of TMDs to reduce their vdW interactions.[131,133,134]

The relationship between the interlayer spacing and the diffusion of alkali metal ions in $MoS_2$ was explored by theoretical calculations.[135,136] With the diffusion pathway of $O_h$ (stable site) → $T_h$ (metastable site) → $O_h$, the diffusion barriers of $Na^+$

 © 2024 The Author(s). Published by the Royal Society of Chemistry

Open Access Article. Published on 19 janvris 2024. Downloaded on 23.02.2025 18:44:43.
This article is licensed under a Creative Commons Attribution-NonCommercial 3.0 Unported Licence.

decrease from 1.14 eV to 0.2 eV with increasing the interlayer spacing from 6.5 Å to 9 Å. In the case of $Li^+$, with the same diffusion pathway, the diffusion barriers decrease continuously from 0.54 eV with increasing the interlayer spacing from 6.5 Å to 7.5 Å. When the interlayer spacing is larger than 7.5 Å, the $T_h$ site becomes more stable than the $O_h$ site, making the diffusion from $O_h$ to $T_h$ endothermic.[137,138] Therefore, the diffusion barriers of $Li^+$ increase slightly to 0.31 eV with increasing the interlayer spacing from 7.5 Å to 9 Å. The relationship between the interlayer spacing and the diffusion of $K^+$ in $MoS_2$ was also explored by Zheng *et al.* with the diffusion path shown in Fig. 5a (the diffusion path of $K^+$ is indicated by the blue dotted line).[136] The results show that the diffusion barriers of $K^+$ decrease from 3.94 eV to 0.045 eV with increasing the interlayer spacing from 6.2 Å to 9.2 Å (Fig. 5b). In general, taking $MoS_2$ as an example, the diffusion barriers of alkali metal ions decrease with increasing the interlayer spacing of TMDs, and the increased interlayer spacing is beneficial for the rapid ion transport kinetics of TMDs.[139,140]

Xu *et al.* summarized the strategies for synthesizing interlayer-expanded TMDs as 'top-down' and 'bottom-up' approaches.[133] Specifically, the methods for expanding interlayer spacing can be divided into two categories: one is the restacking of exfoliated TMD monolayer nanosheets, and the other is to introduce guests or guest precursors into TMD interlayers.[133,141] Du *et al.* restacked $MoS_2$ by an exfoliation and restacking process with enlarged interlayer spacing. The enlarged interlayer spacing of $MoS_2$ provides a larger space for $Li^+$ intercalation and reduces the diffusion barriers of $Li^+$. Consequently, the restacked $MoS_2$ exhibits improved electrochemical performance compared to raw $MoS_2$.[142] In the case of introducing guests or guest precursors into TMD interlayers, they include many foreign species, such as ions, organics, carbon, *etc.*[133,143–145] The intercalated ions are often metal ions and $NH_4^+$.[137,146,147] Zak *et al.* intercalated alkali metals into $MS_2$ (M = W and Mo) nanoparticles by exposing $MS_2$ to alkali metal (Na and K) vapor, and observed a substantial increase (≈3–5 Å) in the interlayer spacing of the intercalated phase.[146] Ma *et al.* reported a multivalent ion intercalation method to construct 3D Co–$MoS_2$ nanoflowers with expanded interlayer spacing. The intercalated $Co^{2+}$ forms S–Co–S covalent bonds and enlarges the maximum interlayer spacing to 1.1 nm, which dramatically reduces the diffusion barriers of $Na^+$.[141] Hu *et al.* expanded the interlayer spacing of $MoS_2$ by intercalating $Na^+$ and $NH_4^+$. The expanded interlayers reduce the charge transfer resistance and provide more active sites for $Na^+$ storage.[147] As for the organic

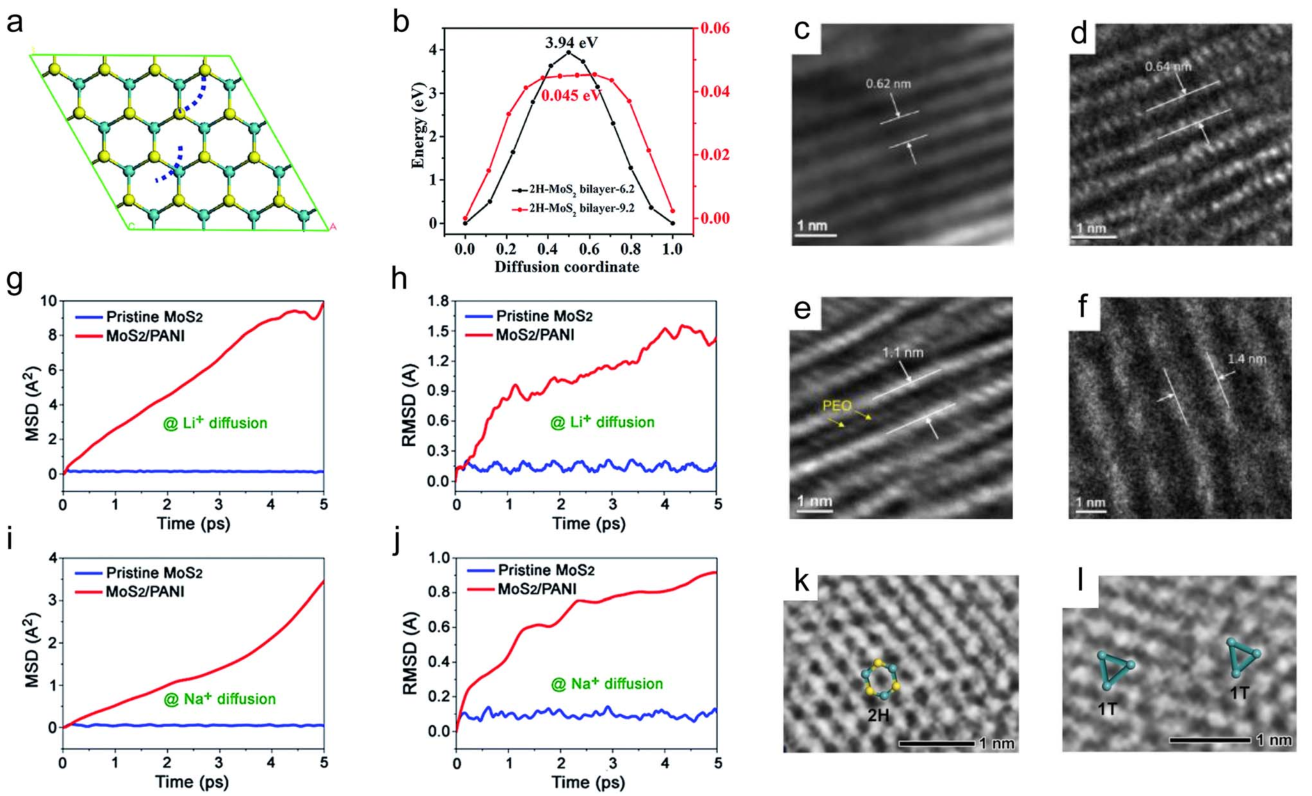


Fig. 5 Interlayer spacing and diffusion of alkali metal-ions. (a) Top view of the optimized $MoS_2/MoS_2$ interface (the blue dotted line indicates the $K^+$ diffusion path). (b) Energy profiles along the diffusion path in the selected interlayer spacing of $MoS_2/MoS_2$. (c and e) The mean square displacement and (d and f) the root mean square displacement of $Li^+/Na^+$ as a function of time of $Li^+/Na^+$ diffusion on the pristine $MoS_2$ nanosheets and the $MoS_2$/PANI hybrid nanosheets. (g–j) High-resolution TEM images show the cross-sectional view of com-$MoS_2$, re-$MoS_2$, $PEO_{1L}$–$MoS_2$, and $PEO_{2L}$–$MoS_2$. High-resolution TEM images and atomic models for (k) 2H-$MoS_2$ and (l) 1T-$MoS_2$, respectively. Reproduced with permission from (a and b) ref. 136. Copyright 2019, Royal Society of Chemistry; (c–f) ref. 46. Copyright 2017, Royal Society of Chemistry; (g–j) ref. 151. Copyright 2015, Elsevier; (k and l) ref. 149. Copyright 2020, Wiley-VCH.

Open Access Article. Published on 19 janvris 2024. Downloaded on 23.02.2025 18:44:43.
This article is licensed under a Creative Commons Attribution-NonCommercial 3.0 Unported Licence.

guests, a large number of organics has been reported that can be intercalated into TMD interlayers,[14,145] such as poly(ethylene oxide) (PEO), polyaniline (PANI), oleylamine, methylamine, polypyrrole, *etc.*[46,47,148–150] Yao and co-workers synthesized PEO-intercalated $MoS_2$ composites (PEO–$MoS_2$) using an exfoliation-restacking method.[151] They prepared 4 samples, commercial $MoS_2$ (com-$MoS_2$), restacked $MoS_2$ without PEO (re-$MoS_2$), and monolayer and bilayer PEO-intercalated $MoS_2$ composites ($PEO_{1L}$–$MoS_2$ and $PEO_{2L}$–$MoS_2$) for comparison. The com-$MoS_2$ shows a sharp diffraction peak located at 14.4°, corresponding to an interlayer spacing of 0.62 nm (Fig. 5c). For re-$MoS_2$, $PEO_{1L}$–$MoS_2$, and $PEO_{2L}$–$MoS_2$, the peaks become broadened and shift to lower angles, indicating the less ordered structures and the larger interlayer spacing. Compared to that of com-$MoS_2$, the interlayer spacing of re-$MoS_2$, $PEO_{1L}$–$MoS_2$, and $PEO_{2L}$–$MoS_2$ is increased to 0.64 nm, 1.1 nm, and 1.4 nm, respectively (Fig. 5d–f). As a result, $PEO_{2L}$–$MoS_2$, with a 160% increase in the interlayer spacing, exhibits the best electrochemical performance due to its greatest improvement in $Na^+$ diffusivity. It is worth pointing out that the addition of excessive PEO will not further increase the interlayer spacing of $MoS_2$. The incorporation of a conducting polymer can not only increase the interlayer spacing but also improve the conductivity of TMDs. Wang *et al.* prepared $MoS_2$/polyaniline (PANI) hetero-structures with enlarged interlayer spacing for $Li^+$ and $Na^+$ storage,[46] and they performed an AIMD simulation of the diffusion of $Li^+$ and $Na^+$ on pristine $MoS_2$ nanosheets and the $MoS_2$/PANI hybrid nanosheets (Fig. 5g–j). The mean square displacement (MSD) and the root mean square deviation (RMSD) values of $Li^+$ and $Na^+$ in $MoS_2$/PANI hybrid nanosheets are both much larger than that in pristine $MoS_2$ nanosheets, suggesting the faster diffusion mobility of $Li^+$ and $Na^+$, which is attributed to the improved conductivity and the enlarged interlayer spacing of $MoS_2$/PANI composites. In the case of the carbon guests, they are usually formed *via* a subsequent carbonization process of $MoS_2$ with pre-intercalated organics.[152–154] For example, Jiang *et al.* prepared a 2D $MoS_2$/mesoporous carbon hybrid nanostructure by annealing the $MoS_2$/polydopamine (PDA) composites.[155] Feng *et al.* synthesized interlayer-expanded $MoS_2$/carbon hetero-aerogels by directly intercalating different polymers (polyethyleneimine and polyethylene glycol) into the $MoS_2$ interlayers before the carbonization process,[156] and the effects of intercalated carbon layers are similar to that of intercalated conducting polymers, such as PANI. In addition, the introduction of foreign species can also induce the phase transformation from the semiconducting phase to the metallic phase, which can enhance the electrical conductivity of Mo and W-based dichalcogenides. Ye *et al.* introduced methylamine into the $MoS_2$ interlayers.[149] The introduction of methylamine can not only expand the interlayer spacing, but also force the transformation of $MoS_2$ from the 2H phase to the 1T phase, resulting in the formation of a metal-semiconducting mixed $MoS_2$ phase (Fig. 5k and l).

The interlayer spacing expansion strategy is also widely used for multivalent ions to enhance their diffusion behaviors in TMDs.[157–160] Similar to the theoretical research of the diffusion behaviors of alkali metal ions in $MoS_2$, the diffusion behaviors of $Mg^{2+}$ in $MoS_2$ with varying interlayer spacing were also

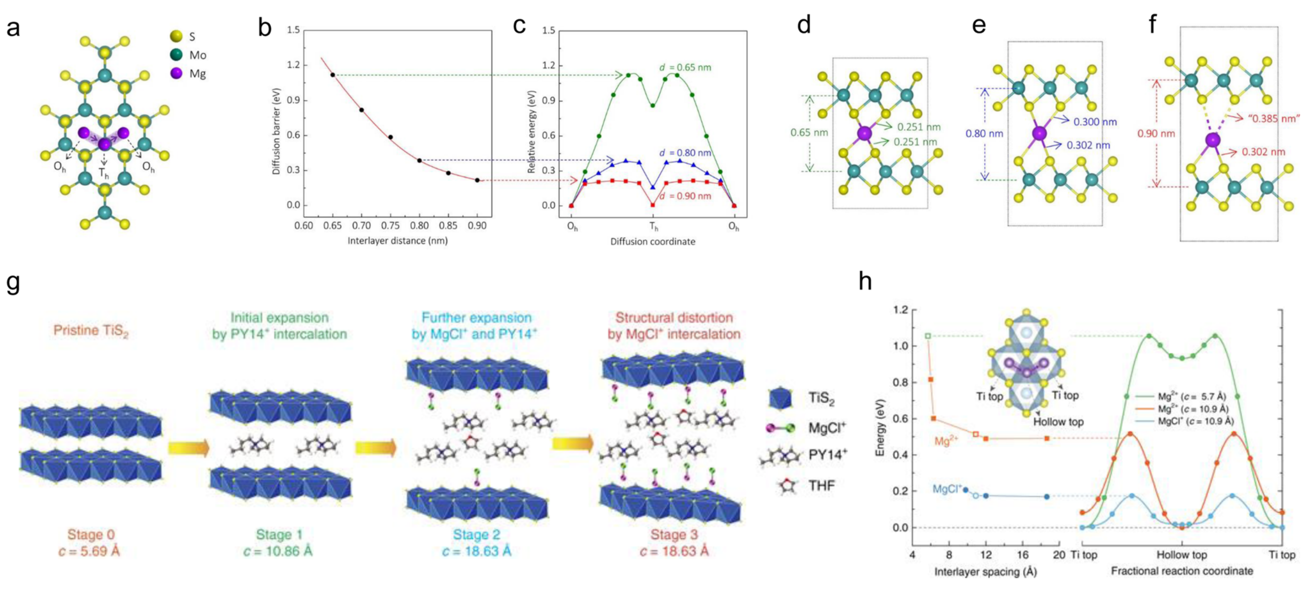


Fig. 6 Mg diffusion in $MoS_2$ and $TiS_2$. (a) Calculated Mg diffusion path in $MoS_2$. (b) The energy barrier for Mg diffusion continuously decreases as the interlayer distance of $MoS_2$ increases. (c) Potential energy diagram for Mg migration at interlayer spacings of $d = 0.65$, 0.80, and 0.90 nm. As the interlayer distance increases from 0.65 nm (d) to 0.80 nm (e) and then 0.90 nm (f), the bond between Mg and $MoS_2$ lengthens and is finally broken on one side. (g) A schematic of structural evolution of $TiS_2$ at different stages of intercalation. (h) First-principles calculations for the diffusion of Mg-ions in $TiS_2$. The energy barrier for the migration of $Mg^{2+}$ and $MgCl^+$ as a function of the interlayer distance of $TiS_2$ at the dilute limit. The diffusion path from a Ti top site to another Ti top site *via* the adjacent hollow top site is shown in the inset. Energy diagrams along the diffusion path for the three representative cases of $Mg^{2+}$ at $c = 5.7$ Å (green), $Mg^{2+}$ at $c = 10.9$ Å (orange), and $MgCl^+$ at $c = 10.9$ Å (cyan). Reproduced with permission from (a–f) ref. 161. Copyright 2015, American Chemical Society; (g and h) ref. 162. Copyright 2017, Springer Nature.

 © 2024 The Author(s). Published by the Royal Society of Chemistry

Open Access Article. Published on 19 janvris 2024. Downloaded on 23.02.2025 18:44:43. This article is licensed under a Creative Commons Attribution-NonCommercial 3.0 Unported Licence.

explored by Yao and co-workers in the diffusion pathway of $O_h \rightarrow T_h \rightarrow O_h$ (Fig. 6a).[161] As shown in Fig. 6b and c, as the interlayer spacing increases from 0.65 nm to 0.9 nm, the diffusion barriers continuously decrease from 1.12 eV to 0.22 eV. The reason behind the continuous decrease in the diffusion barriers is the gradually weaker bonding between Mg and one of the two layers of $MoS_2$ (Fig. 6d–f). It is worth pointing out that traditional interlayer engineering uses the TMDs (whose interlayer spacing has already been expanded) as electrode materials, which needs a pre-processing step. Yao and co-workers further developed an *in situ* interlayer expansion strategy for $TiS_2$ for fast $MgCl^+$ storage *via* electrolyte engineering.[162] As shown in Fig. 6g, they added PY14Cl into the electrolyte, and $Py14^+$ expanded the interlayer of $TiS_2$ *in situ* first during discharging in stage 1. From stage 1 to stage 3, a large amount of $MgCl^+$ is intercalated continuously with a small amount of THF molecules, resulting in greatly improved electrochemical performance. The theoretical calculations show that for the same interlayer spacing, the diffusion barriers of $MgCl^+$ are always lower than that of $Mg^{2+}$, indicating the advantage of $MgCl^+$ storage (Fig. 6h). For $Zn^{2+}$ storage, Huang *et al.* intercalated PANI into $MoS_2$ interlayers to expand the interlayer spacing.[49] The intercalated PANI expands the diffusion channels of $Zn^{2+}$ and reduces the electrostatic interaction between $Zn^{2+}$ and $MoS_2$, thus enhancing the electrochemical performance. Cui *et al.* introduced anionic organic layers (sodium dodecyl benzene sulfonate) into $WSe_2$ to form superlattice-type $WSe_2$ (S-$WSe_2$) for $Al^{3+}$ storage. The interlayer spacing expansion strategy makes S-$WSe_2$ more active as a cathode in rechargeable Al batteries.[163]

In short, the interlayer spacing expansion strategy can comprehensively reduce the diffusion barriers of metal-ions in TMDs. The enlarged specific surface, the transformation of TMDs from the semiconducting phase to the metallic phase, the reduced lattice stress, and the improved electrical conductivity of TMDs are also observed.

### 3.4 Heteroatom doping

Similar to introducing defects into TMDs, heteroatom doping is also an effective strategy to modulate the local properties of TMDs, which has been reported to improve the conductivity, expand the interlayer spacing, and enhance the atom adsorption capacity of TMDs.[164–166] The doped atoms can be divided into two categories: metal heteroatoms, such as Mn, Zn, Fe, Co, Ni, Cu, Re, Pd, Sn, and Au,[50,167–174] and non-metal heteroatoms, such as N, O, As, P, F, Cl, Br, I, H, and B.[51,170,174–176] The dopant type is an important factor that affects the electrochemical performance of TMDs.

Sun *et al.* theoretically investigated the properties of heteroatom-doped monolayer $MoS_2$ and the adsorption and diffusion of Li on heteroatom-doped $MoS_2$ by substituting S with some nonmetallic elements (N, P, As, F, Cl, and I) and Mo with some metallic elements (Fe, Co, Ni, Cu, and Zn) (Fig. 7a–f).[177] The DOS of monolayer $MoS_2$ with different doping elements is shown in Fig. 7a and b. Although the doped monolayer $MoS_2$ still exhibits semiconducting characteristics, the conductivity is improved to varying degrees. For metallic heteroatom doping, substituting Mo with Co, Ni, Cu, and Zn makes monolayer $MoS_2$ exhibit p-type conducting behavior. For non-metallic heteroatom doping, substituting S with N, P, and As also makes monolayer $MoS_2$ exhibit p-type conducting behavior due to their one less valence electron than S. In contrast, substituting S with F, Cl, and I makes monolayer $MoS_2$ exhibit n-type conducting behavior. In the case of studying the adsorption of Li on heteroatom doped monolayer $MoS_2$, two types of adsorption sites, the hollow site (H) and the top site above Mo (T), and the position of the adsorption sites as a function of distance from the doped site are considered. The adsorption energies of Li on pristine monolayer $MoS_2$ are $-0.95$ and $-1.24$ eV for H and T sites. For all doped elements studied in this work,[177] higher adsorption energies are observed near the doped sites, indicating the stronger bonding between Li and doped monolayer $MoS_2$, and the adsorption energies decrease with increasing the distance from the adsorption sites to the doped sites. In addition, for non-metallic heteroatom doping, the adsorption energies of Li on N, P, and As doped monolayer $MoS_2$ are higher than that on the other three elements (F, Cl, and I) doped monolayer $MoS_2$, indicating that p-type doping is more beneficial for improving the adsorption of Li. This phenomenon can also be found in the case of metallic heteroatom doping. The diffusion energy barriers of Li on doped monolayer $MoS_2$ were explored with the diffusion pathways shown in Fig. 7c and e. Similar to the effects of defects, when Li diffuses towards the doped sites, the diffusion energy barriers decrease, especially near the doped sites (Fig. 7d and f). In contrast, the diffusion energy barriers increase when Li diffuses away from the doped sites, suggesting the strong adsorption ability of the doped sites. For diffusion pathways far from the doped sites, the diffusion energy barriers will not be affected by the doped heteroatoms. Similarly, the adsorption and diffusion of alkali metals on heteroatom-doped monolayer $TiS_2$ were then explored by Tian *et al. via* theoretical calculations (Fig. 7g–j).[178] For the adsorption properties of alkali metals, monolayer $TiS_2$ doped with C, N, and P (corresponding to p-type doping) exhibits higher adsorption energies (Fig. 7g), which is the same as the results obtained by Sun *et al.*[177] And the adsorption energies of alkali metals on $TiS_2$ with and without doped heteroatoms follow the order of Li > K > Na, which is thought to be affected by both the atomic radius and electronegativity. With the diffusion pathway shown in Fig. 7h and i, the diffusion energy barriers of alkali metals on heteroatom doped monolayer $TiS_2$ increase to varying degrees compared to that on pristine monolayer $TiS_2$ (Fig. 7j). But all of them are less than 0.6 eV, which assures the moderate diffusion kinetics of alkali metals on heteroatom doped monolayer $TiS_2$. The calculation results also show that the diffusion energy barriers follow the order of K < Na < Li, and this tendency has also been observed in other materials.[179–181]

From the standpoint of theoretical calculations, it can be concluded that heteroatom doping enhances the conductivity and improves the adsorption capacity of TMDs for alkali metals. Although the diffusion energy barriers of alkali metals on TMDs increase, the moderate values can still assure moderate

Open Access Article. Published on 19 janvris 2024. Downloaded on 23.02.2025 18:44:43.
This article is licensed under a Creative Commons Attribution-NonCommercial 3.0 Unported Licence.

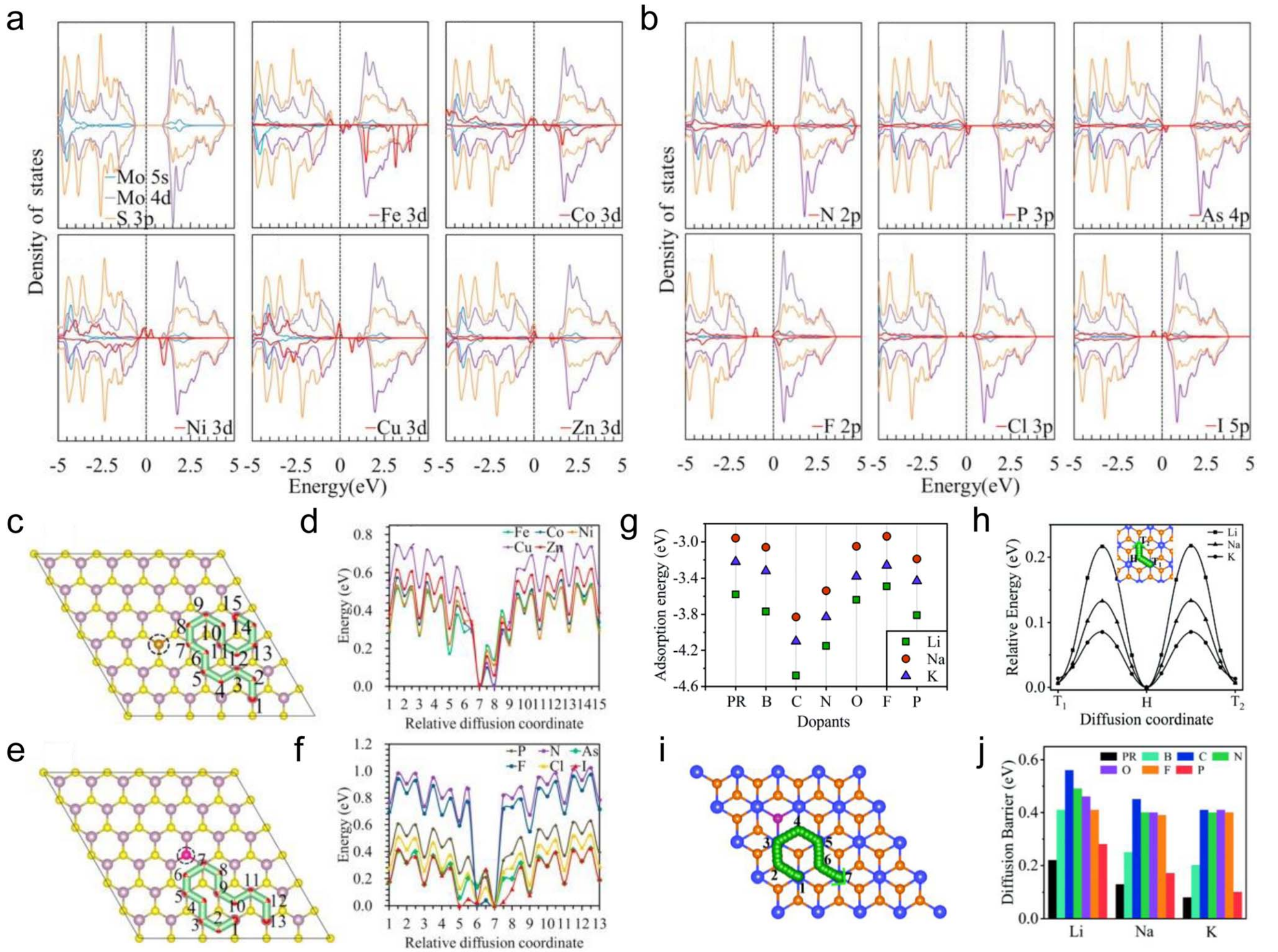


Fig. 7 Density of states, dopant absorption energies, and diffusion pathways. (a) The projected density of states for pristine and monolayer $MoS_2$ with substitution of Mo with Fe, Co, Ni, Cu, and Zn. (b) The projected density of states for monolayer $MoS_2$ with substitution of S with N, P, As, F, Cl, and I in monolayer $MoS_2$. Diffusion path and corresponding diffusion energy profiles for Li on (c and d) metal (e and f) nonmetal atom-doped monolayer $MoS_2$. (g) The lowest adsorption energies for Li, Na, and K adsorbed on monolayer $TiS_2$ without and with B, C, N, O, F, and P heteroatom doping. (h) Diffusion pathway and energy profiles for alkali metals on pristine monolayer $TiS_2$. (i) Diffusion pathway of alkali metals on heteroatom doped monolayer $TiS_2$. (j) The overall diffusion energy barriers for alkali metals on pristine and heteroatom-doped $TiS_2$. Reproduced with permission from (a–f) ref. 177. Copyright 2018, American Chemical Society; (g–j) ref. 178. Copyright 2021, Royal Society of Chemistry.

diffusion kinetics. For example, Qin *et al.* developed N-doped $MoS_2$ nanosheets for $Li^+$ storage. They found that the N-doped $MoS_2$ nanosheets exhibit an improved conductivity of *ca.* $1.6 \times 10^{-4}$ S $m^{-1}$, while it is only *ca.* $1.1 \times 10^{-5}$ S $m^{-1}$ for pristine $MoS_2$ nanosheets.[182] Xie *et al.* prepared Co-doped $MoS_2$ for $Na^+$ storage.[183] The Co-doping improves the conductivity of $MoS_2$ and enhances the adsorption capacity of $MoS_2$ for $Na^+$. After being combined with N-doped graphene, Co-doped $MoS_2$ exhibits higher specific capacity and better rate performance. The doping concentration is an important factor in maximizing the advantages of doping. Zhao *et al.* explored the optimal concentration by injecting different amounts of Mo into $VS_2$,[184] and 5% Mo-doping concentration exhibits the best electrochemical performance (Fig. 8a and b). Upon further increasing the doping concentrations, the electrochemical performance worsens and is almost the same as that of pristine $VS_2$. This phenomenon is attributed to the distortion of atomic structures as a result of excessive doping.[185] Apart from the single heteroatom doping, Zhang *et al.* explored $NbS_2$ nanosheets with varying concentrations of M (M = Fe, Co, Ni) and Se codopants to store $Li^+$ and $Na^+$ (Fig. 8c).[186] After optimizing the doping ratios, $Fe_{0.3}Nb_{0.7}S_{1.6}Se_{0.4}$ exhibits the best electrochemical performance. In addition to being able to manipulate the energy band structures of TMDs, the doping of heteroatoms can also lead to the transformation of Mo and W-based dichalcogenides from the semiconducting phase to the metallic phase, which can further enhance the conductivity. Wang *et al.* prepared N-doped $MoS_2$ for Li storage.[187] And N-doping induces the transformation of $MoS_2$ from the 2H to the 1T phase (Fig. 8d), thus enhancing the conductivity of $MoS_2$. He *et al.* developed a plasma-assisted method to introduce highly concentrated P-doping to trigger the phase transformation of $MoSe_2$.[109] The Se vacancies ($V_{Se}$) induced by plasma treatment lead to the low crystallinity and structural instability of 2H-

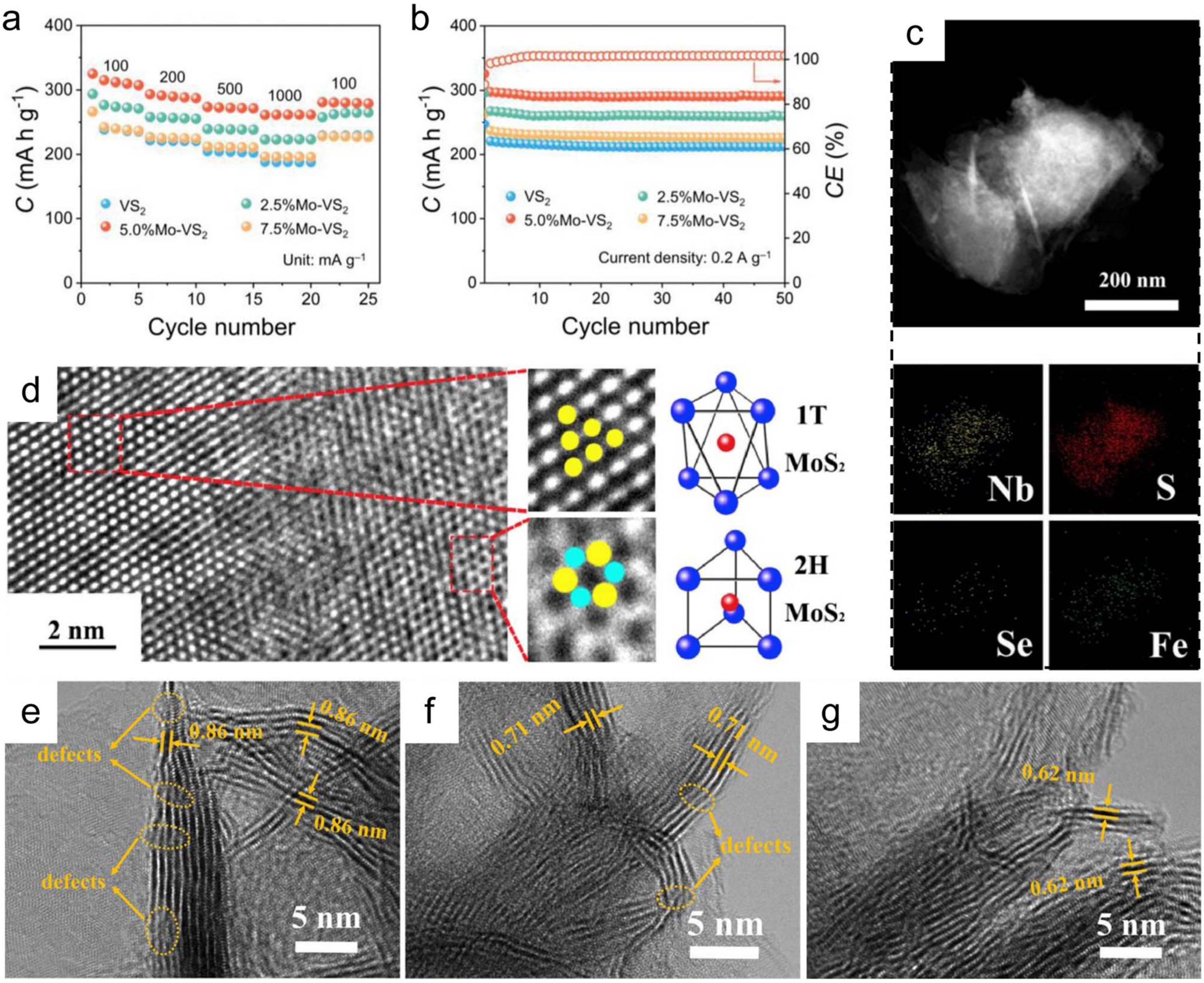


Fig. 8 Electrochemical performance and role of dopants. (a) Rate capability for bare $VS_2$, 2.5% Mo–$VS_2$, 5.0% Mo–$VS_2$, and 7.5% Mo–$VS_2$ cathodes at 0.1–1.0 A $g^{-1}$. (b) Cycling performance for bare $VS_2$, 2.5% Mo–$VS_2$, 5.0% Mo–$VS_2$, and 7.5% Mo–$VS_2$ cathodes at 0.2 A $g^{-1}$. (c) Mapping of $Fe_{0.3}Nb_{0.7}S_{1.6}Se_{0.4}$ nanosheets. (d) High-resolution TEM images of the synthetic composite and simulated image of (up) 1T and (down) 2H-$MoS_2$ (S, blue; Mo, red). High-resolution TEM images of N-doped 1T-$MoS_2$ (e), pure 1T-$MoS_2$ (f), and pure 2H-$MoS_2$ (g). Reproduced with permission from (a and b) ref. 184. Copyright 2023, Wiley-VCH; (c) ref. 186. Copyright 2017, American Chemical Society; (d) ref. 187. Copyright 2017, Elsevier; (e–g) ref. 188. Copyright 2021, American Chemical Society.

$MoSe_2$, which decreases the energy barriers of phase transformation and initializes the phase transformation process. Then, the high concentration of P-doping induced by $V_{Se}$ prefers to donate electrons to Mo than Se, thereby triggering and stabilizing the formation of 1T phase $MoSe_2$ with a high transition efficiency of 91%.

For multivalent ion storage, Sheng *et al.* prepared N-doped 1T phase $MoS_2$ for aqueous $Zn^{2+}$ batteries.[188] Although 1T-$MoS_2$ exhibits a larger interlayer spacing than 2H-$MoS_2$ (Fig. 8f and g), they found that N-doping could further increase the interlayer spacing of 1T-$MoS_2$ (Fig. 8e), thus effectively decreasing the diffusion barriers of $Zn^{2+}$ in $MoS_2$. Li *et al.* introduced O-doping and defects into $MoS_2$ for $Zn^{2+}$ storage.[52] O-doping increases the interlayer spacing and cooperates with structural defects to induce the transformation of $MoS_2$ from the 2H phase to the 1T phase,[51] resulting in improved $Zn^{2+}$ diffusion kinetics, hydrophilicity, and conductivity of $MoS_2$.

In short, heteroatom doping can enhance the conductivity, improve the metal adsorption ability, induce phase transformation, and expand the interlayer spacing of TMDs. Different types of doping exhibit different effects.

### 3.5 Alloy engineering

TMD alloys have been the subject of active research in energy conversion and storage. Unlike the broad selection of heterogeneous elements in doping engineering, the introduced and replaced elements are congeneric in alloy engineering. With a general formula of $MX_{2(1-x)}X'_{2x}$ or $M_{1-x}M'_xX_2$, TMD alloys exhibit intriguing properties when the ratios of the components are changed.

Open Access Article. Published on 19 janvris 2024. Downloaded on 23.02.2025 18:44:43.
This article is licensed under a Creative Commons Attribution-NonCommercial 3.0 Unported Licence.

Open Access Article. Published on 19 janvris 2024. Downloaded on 23.02.2025 18:44:43.
This article is licensed under a Creative Commons Attribution-NonCommercial 3.0 Unported Licence.

Among $MX_{2(1-x)}X'_{2x}$ alloys, $MoS_{2(1-x)}Se_{2x}$ is the representative one and has been widely studied. Ersan *et al.* studied the adsorption and diffusion of Li on $MoS_{2(1-x)}Se_{2x}$ monolayers, where $x$ varied from 0 to 1 (Fig. 9a and b).[189] With the diffusion pathway shown in Fig. 9a, $MoS_2$ and $MoSe_2$ systems exhibit two symmetrical absolute energy maxima, an absolute energy minimum and a local energy minimum. The diffusion energy barriers of Li on $MoS_2$ and $MoSe_2$ are 0.194 and 0.237 eV. When $x$ changes from 0.33 to 0.66, due to the introduction of congeneric elements, two asymmetrical energy maxima are observed, including an absolute maximum and a local energy maximum, and there are still one local and one absolute minimum in the case of $x = 0.33$ and 0.66. For $x = 0.5$, two local minima and one absolute minimum are observed. The diffusion energy barriers are 0.319, 0.541, and 0.391 eV for $MoS_{2(1-x)}Se_{2x}$ alloys with $x =$ 0.33, 0.5, and 0.66. From the calculations, it can be observed that Li prefers to bind with S. Although the diffusion energy barriers of these alloys increase, they are not very high values that are still acceptable for assuring moderate Li diffusion kinetics. The penetration barriers were also explored with varying $x$ values (Fig. 9b). The results show that the penetration energy barriers decrease with increasing $x$ from 0 to 1, indicating that the increasing concentration of Se is beneficial for the penetration of Li. However, a barrier energy of 1.283 eV is still large. One of the reasons may be attributed to the increased crystal constant with increasing Se concentration.

Among $M_{1-x}M'_xX_2$, the $Mo_{1-x}W_xS_2$ alloys have received much attention. Barik *et al.* explored monolayer $Mo_{1-x}W_xS_2$ as anode materials for Li storage *via* theoretical calculations (Fig. 9c–j).[190] For pristine monolayer $Mo_{1-x}W_xS_2$, the DOS and

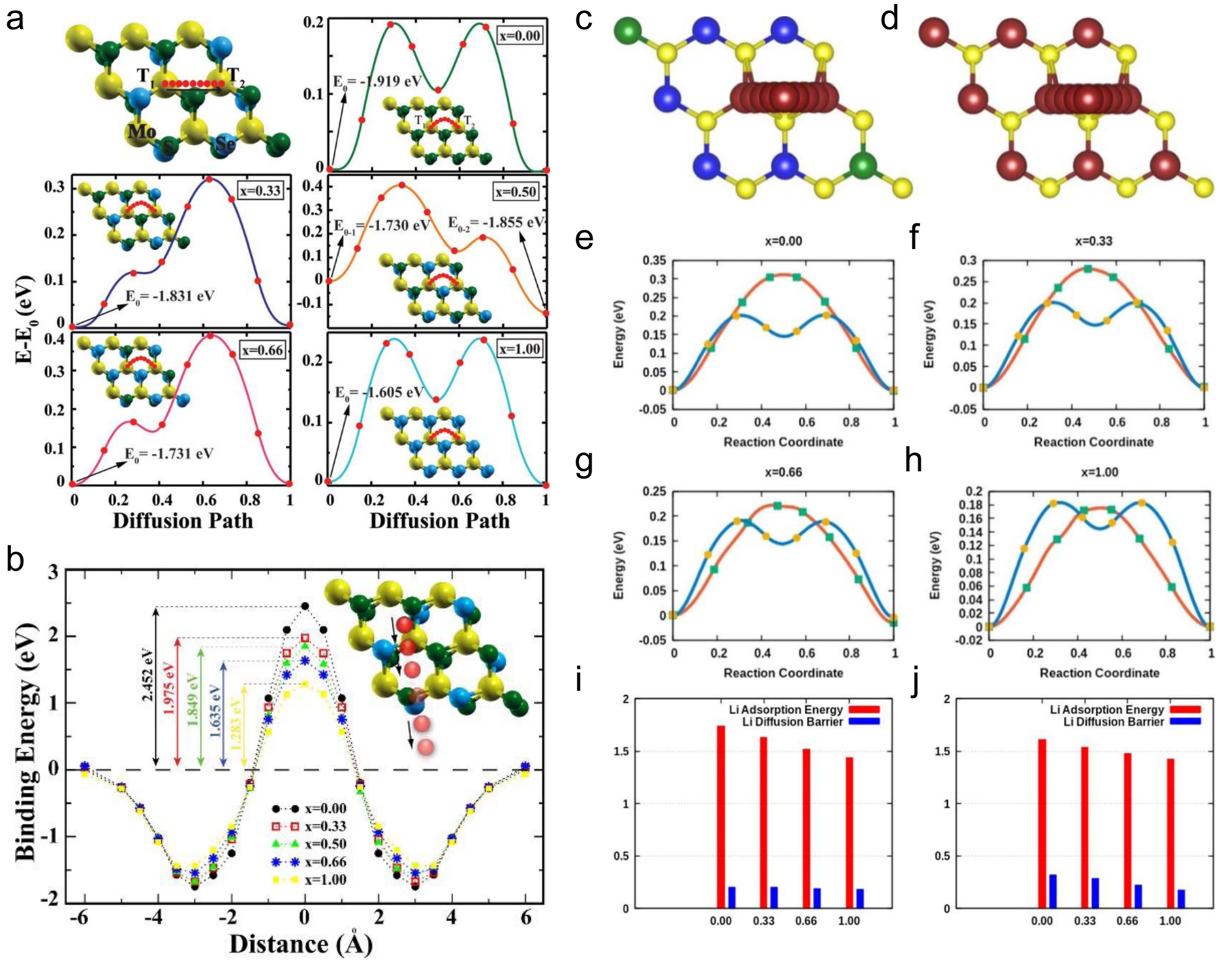


Fig. 9 Diffusion path and binding energies of Li in monolayer TMDs. (a) Lowest energy diffusion paths of a single lithium atom and calculated energy profiles along the paths for one Li atom-adsorbed on the TMD monolayer. (b) Binding energies of a single lithium atom when it approaches and penetrates bare $MoS_{2(1-x)}Se_{2x}$ monolayers from infinity. Schematic representation of the Li diffusion path in the $Mo_{1-x}W_xS_2$ alloy of $x = 0.33$ from one top position to another through the hollow site. (c) Bare surface and (d) lithiated surface. The blue, green, yellow, and maroon balls denote Mo, W, S, and Li atoms, respectively. (e–h) Energy profiles for lithium diffusion on monolayer $Mo_{1-x}W_xS_2$. The blue line indicates a bare surface, and the red line indicates a lithiated surface. Li adsorption energies and diffusion barriers on monolayer $Mo_{1-x}W_xS_2$ compared to different compositions of $x$. (i) Migration of Li on the bare surface and (j) migration of Li on the lithiated surface. Reproduced with permission from (a and b) ref. 189. Copyright 2015, American Chemical Society; (c–j) ref. 190. Copyright 2018, American Chemical Society.

 © 2024 The Author(s). Published by the Royal Society of Chemistry

Open Access Article. Published on 19 janvris 2024. Downloaded on 23.02.2025 18:44:43. This article is licensed under a Creative Commons Attribution-NonCommercial 3.0 Unported Licence.

the band gaps do not change much with different ratios of Mo and W. After lithiation, the conduction band minima of monolayer $Mo_{1-x}W_xS_2$ move towards the Fermi level, suggesting the formation of the metallic phase, which is consistent with the fact that the intercalation of alkali metal ions into Mo and W-based dichalcogenides can induce the formation of the metallic phase.[62,108] With the diffusion pathway shown in Fig. 9c and d, they studied the diffusion energy barriers of Li on pristine and lithiated $Mo_{1-x}W_xS_2$ (Fig. 9e–h).[190] The pristine $MoS_2$ and $WS_2$ systems exhibit two symmetrical absolute maxima. However, the two maxima are not symmetrical in the case of alloys. The maximum at the $T_{Mo}$ site is always slightly higher than that at the $T_W$ site, indicating the stronger bonding interaction between Mo and Li. The lithiated $Mo_{1-x}W_xS_2$ systems exhibit similar characteristics to pristine $Mo_{1-x}W_xS_2$ systems except for the disappearance of the local energy minima due to the repulsion between Li atoms. The Li adsorption and its diffusion energy barriers in pristine and lithiated $Mo_{1-x}W_xS_2$ indicate that they all decrease with increasing W ratios (Fig. 9i and j).

Different from the studies performed by Ersan and Barik *et al.*,[189,190] Chaney and coworkers performed a comprehensive study of the adsorption and diffusion of Li on Janus Mo/WXY (X, Y = S, Se, Te), where the ratio of X and Y was fixed at 1 : 1.[191] According to the adsorption energy results of both regular and Janus TMDs (Fig. 10a and b), it can be concluded that the binding interaction between chalcogen and Li follows the order of S > Se > Te, and for Mo and W, the binding interaction follows the order of Mo > W. The diffusion of Li on regular and Janus TMDs indicates that the diffusion barriers of Li on the X side of Janus MXYs are comparable to that on $MX_2$ (Fig. 10c and d), while the diffusion barriers of Li on the Y side of Janus MXYs are always lower than that on the X side due to the weaker interaction between Li and Y.

According to the calculations, alloying is an effective strategy to balance the adsorption and diffusion of ions on TMDs. This also applies to some other properties for $MX_{2(1-x)}X'_{2x}$ under similar conditions of the same ion storage capacity. The alloys will balance the theoretical specific capacity of TMD electrodes. For example, the relative atomic mass of S is lower than that of Se. Therefore, increasing the content of S in $MSe_{2(1-x)}S_{2x}$ will reduce the relative molecular mass of $MSe_{2(1-x)}S_{2x}$. However, the ion storage capacity of $MSe_{2(1-x)}S_{2x}$ will not change with the variation of the ratios of Se and S due to the same ion storage mechanism in $MoS_2$ and $MoSe_2$. As a result, the theoretical specific capacity of $MSe_{2(1-x)}S_{2x}$ will increase with increasing the content of S.[192,193] Although increasing the Se content would reduce the theoretical specific capacity of $MSe_{2(1-x)}S_{2x}$, Se has a larger atomic radius than S, which can enlarge the interlayer spacing of $MSe_{2(1-x)}S_{2x}$, resulting in reduced ion diffusion barriers (Fig. 11a and b).[54,194,195] In addition to the increased specific capacity and the enlarged interlayer spacing, the incorporation of S or Se can also induce the structural rearrangement and the electron redistribution of $MSe_{2(1-x)}S_{2x}$, leading to the formation of abundant anion vacancies and the metallic phase, which can increase the active adsorption sites and enhance the conductivity of $MSe_{2(1-x)}S_{2x}$.[56,196–198] He *et al.* fabricated $MoS_{2(1-x)}Se_{2x}$ alloys through partial substitution of S for Se in $MoSe_2$. They found that the alloying process can generate anion vacancies, and the vacancy concentration can be adjusted by tuning the ratios of S and Se.[55] With a S : Se ratio close to 1 : 1, the largest vacancy concentration and the best electrochemical performance are achieved (Fig. 11c–e). Huang *et al.* synthesized MoSSe@rGo for $Na^+$ storage,[198] and in their Raman spectra, the 1T-$MoSe_2$ and 1T-$MoS_2$ modes were observed in both MoSSe and MoSSe@rGO, indicating the formation of a metallic phase by the alloying process (Fig. 11f). For $M_{1-x}M'_xX_2$, a similar phenomenon was also observed.[199,200] Besides, there is an additional possibility that introducing the M elements from metallic phase $MX_2$ into semiconducting phase $M'X_2$ may endow $M_{1-x}M'_xX_2$ with interesting properties. Our group explored this possibility by introducing V into $MoS_2$ to form $Mo_{1-x}V_xS_2$ for Li storage.[201] The introduction of V into $MoS_2$ makes $Mo_{1-x}V_xS_2$ exhibit semi-metallic conductivity, making $Mo_{1-x}V_xS_2$ exhibit enhanced conductivity and better electrochemical performance than pristine 2H-$MoS_2$.

As discussed above, the different elements in $MX_{2(1-x)}X'_{2x}$ or $M_{1-x}M'_xX_2$ alloys have different influences. Therefore, it is important to manipulate the $x$ values to optimize the electrochemical performance of TMD alloys. However, the optimal $x$ values reported by different studies vary. For example, He and Yu *et al.* found that the electrochemical performance of $MoS_{2(1-x)}Se_{2x}$ becomes the best when $x = 0.5$.[55,197] However, Cai and coworkers believed that $x = 0.25$ is the optimal value for the $MoS_{2(1-x)}Se_{2x}$ alloys.[202] For $Mo_{1-x}W_xS_2$, a similar issue also exists.[53,203] The optimal values of $x$ may be due to the other factors that can also affect the electrochemical performance of TMD alloys, such as the morphology and the types of stored ions, which need comprehensive and detailed studies.

In short, alloy engineering is expected to balance different properties of TMDs, such as the metallic phase formation and the interlayer spacing enlargement. Defect introduction can also be achieved by alloying; however, the issue that needs to be clarified is determining the optimal $x$ value and its influencing factors in TMD alloy systems.

### 3.6 Bond modulation

Different from the several mainstream molecular modulation strategies discussed above, the bond modulation strategy focuses on the impact of chemical bonds on the properties of TMDs, including bond length, bond angle, bond energy, and additionally created chemical bonds.[170,204] For example, by manipulating the bond length, the interlayer spacing can be modulated,[164,205] and the enhanced bond energy can stabilize the intercalation reaction, although it will make it more difficult for the conversion reaction to occur.[168,169] The additional chemical bond formation in TMDs shows more possibilities in comparison and has therefore been studied more extensively. For instance, covalent interactions usually exist between the introduced guests and the transition metals or chalcogens in TMDs so they can be stably bonded at room temperature and modulate the TMDs' properties.[145,154] Our group has demonstrated that the introduced Se atoms between the interlayers of

Open Access Article. Published on 19 janvris 2024. Downloaded on 23.02.2025 18:44:43.
This article is licensed under a Creative Commons Attribution-NonCommercial 3.0 Unported Licence.

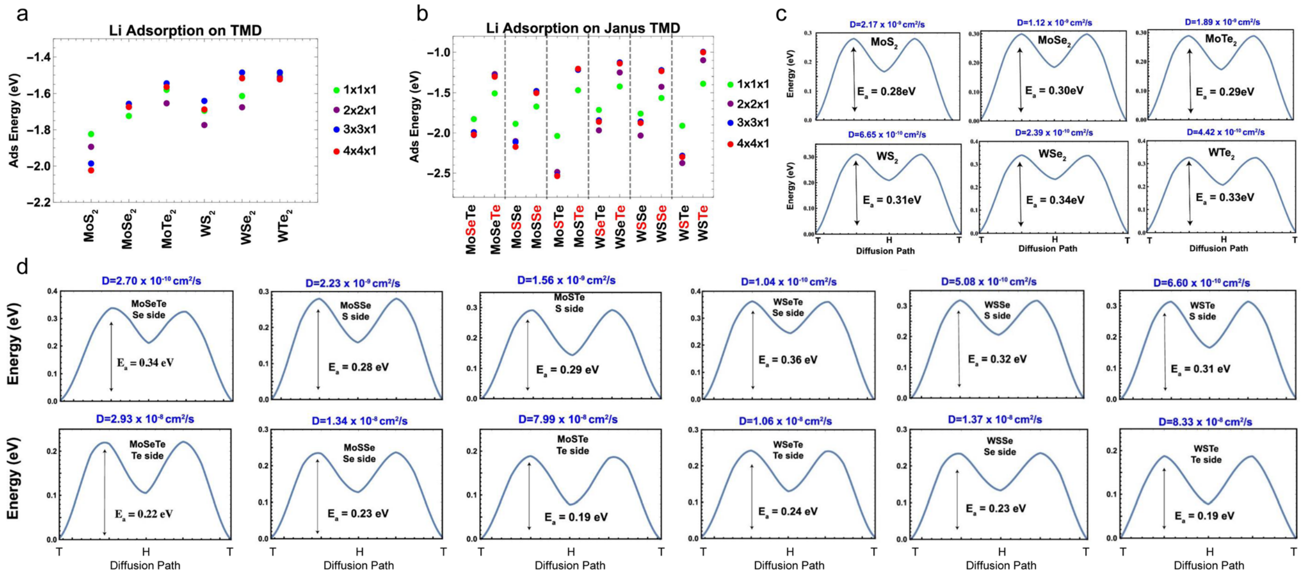


Fig. 10 Adsorption energies for a Li atom over metal-top sites of all supercell sizes. (a) Mo- and W-based TMDs and (b) top and bottom sides of Janus structures. The red color on the chalcogen atom of Janus structures on the *x*-axis labeling indicates the side on which the Li atom is adsorbed. (c) Activation energy barriers for Li atom diffusion for regular TMD-$MX_2$ (M = Mo, W; X = S, Se, Te), calculated with the nudged elastic band (NEB) method simulations. (d) Activation energy barriers for Li atom diffusion for Janus TMD MXY (M = Mo, W; X/Y = S, Se, Te), calculated with NEB simulations. Reproduced with permission from (a–d) ref. 191. Copyright 2021, American Chemical Society.

$MoSe_2$ form covalent Se–Se bonds with the Se in $MoSe_2$,[58] and the covalent Se–Se bonds not only enlarge the interlayer spacing of $MoSe_2$ but also prevent the Se shuttle effects. The S–Co–S covalent bonds formed by intercalating Co into $MoS_2$ interlayers can induce the formation of the 1T phase, expand the interlayer spacing of $MoS_2$, and serve as electrical pathways to accelerate

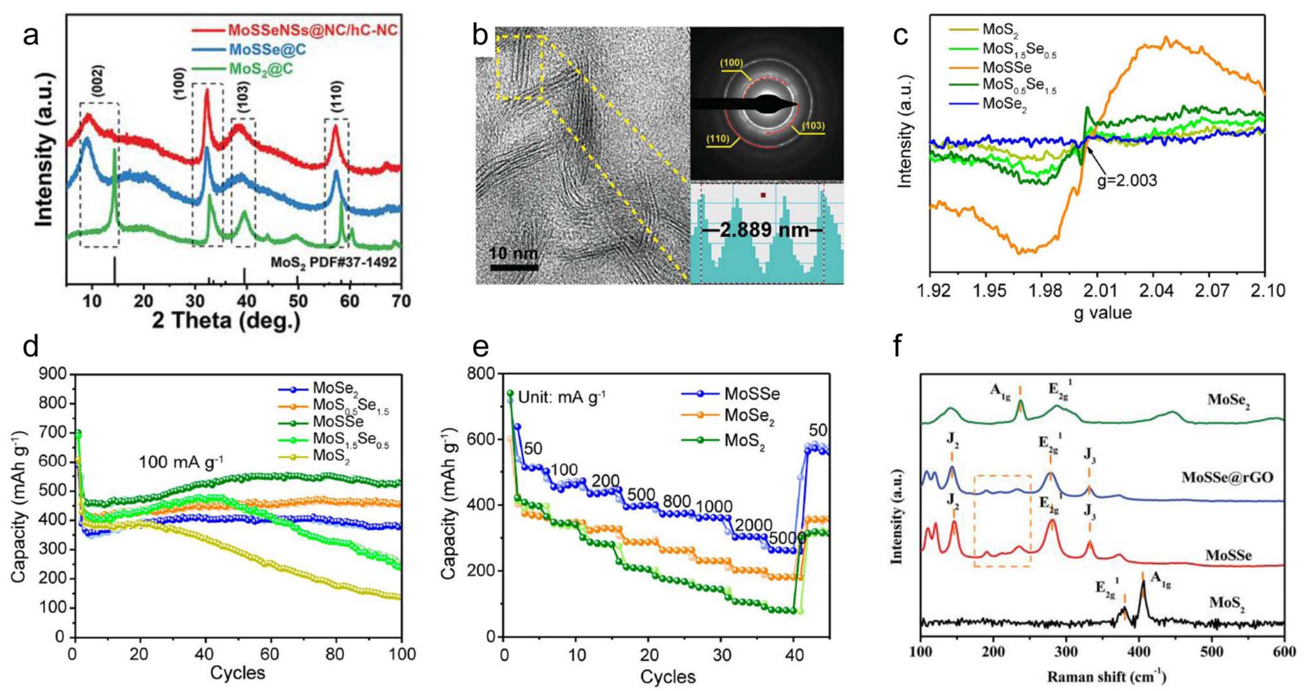


Fig. 11 Structural, electrochemical, and Raman properties of $MoS_{2(1-x)}Se_{2x}$ alloys. (a) XRD patterns of MoSSeNSs@NC/hC-NC, MoSSe@C and $MoS_2$@C. (b) HRTEM image of MoSSeNSs@NC/hC-NC. (c) EPR results of $MoSe_2$, MoSSe, and $MoS_2$. (d) Cycling performance at 100 mA $g^{-1}$ for all the as-prepared samples. (e) Rate capability of $MoSe_2$, MoSSe, and $MoS_2$. (f) Raman spectra of as-prepared MoSSe@rGO, MoSSe, $MoS_2$, and $MoSe_2$ samples. MoSSeNSs@NC/hC-NC: MoSSe nanosheets supported on hollow cubic N-doped carbon. Reproduced with permission from (a and b) ref. 195. Copyright 2021, Wiley-VCH; (c–e) ref. 55. Copyright 2019, American Chemical Society; (f) ref. 198. Copyright 2020, Wiley-VCH.

 © 2024 The Author(s). Published by the Royal Society of Chemistry

Open Access Article. Published on 19 janvris 2024. Downloaded on 23.02.2025 18:44:43.
This article is licensed under a Creative Commons Attribution-NonCommercial 3.0 Unported Licence.

interlayer charge transfer, thus greatly improving the electrochemical performance of $MoS_2$.[141] In addition, introducing additional chemical bonds by incorporating additional atoms into TMDs can also lead to interesting phenomena. For example, Zhang *et al.* prepared unusual red $MoSe_2$ nanosheets by introducing an oxygen gradient on the surface of $MoSe_2$ nanosheets and forming Mo–O bonds.[57] The formation of Mo–O bonds induces the formation of high valence Mo, thereby regulating the band gap of red $MoSe_2$ and enhancing its electrical conductivity. A similar enhanced electrical conductivity was also observed when incorporating P and N atoms into TMDs due to the formation of M–P and M–N bonds.[109,182,206]

In short, the bond modulation strategy modulates the properties of TMDs from a chemical bonding viewpoint. The bond length, bond angle, bond energy, and additional chemical bonding all impact the electrochemical performance of TMDs. However, they have not received widespread attention yet, and some systematic studies are lacking, thus needing further exploration in the future.

## 4. Summary and perspectives

In summary, this review outlines the basic properties of TMDs and discusses the molecular modulation strategies of TMDs by combining computational and experimental studies towards their application in metal ion batteries. In brief, due to the different coordination and stacking sequences of transition metals, TMDs show polymorphs and stacking polytypes. Among them, 1T and 2H phase TMDs are widely studied in metal ion batteries. The coordination environment of transition metals and the filling states of their d orbitals determine the electrical properties of TMDs. When the orbitals are fully occupied, semiconducting behaviour is exhibited, such as in 2H-$MoS_2$ and 2H-$MoSe_2$. When the orbitals are partially filled, metallic conductivity is exhibited, such as in 2H-$NbS_2$ and 1T-$VS_2$. In addition, the chalcogen atoms can also affect the electronic properties of TMDs, although their influence is not significant. When TMDs are used as alkali metal-ion battery electrodes, reversible intercalation and extraction reactions occur at a relatively high cutoff voltage (~1 V). As the intercalation process continues, the subsequent reaction mechanism depends on the M–X bond strength of TMDs. If the M–X bonding interactions are stronger than the A–$MX_2$ interactions, reversible intercalation and extraction reactions, such as in $TiX_2$ and $NbX_2$, will continue. In contrast, conversion reactions will occur if the M–X bonding interactions are weaker than the A–$MX_2$ interactions, and the reversibility of the conversion reactions depends on the dynamic properties of TMDs. Excellent dynamic properties of TMDs contribute to reversible conversion reactions, such as in $VX_2$, while poor dynamic properties of TMDs lead to irreversible conversion reactions, such as in $MoX_2$, $WX_2$, and $ReX_2$. Only intercalation and extraction reactions have been reported when TMD electrodes are used in multivalent-ion batteries.

Several molecular modulation strategies of TMDs, including phase engineering, defect engineering, interlayer spacing expansion, heteroatom doping, alloy engineering, and bond modulation, are also discussed. By combining theoretical and experimental studies, the basic mechanisms of different molecular modulation strategies and their specific effects on the properties of TMDs for storing metal ions are summarized, (1) phase engineering aims at improving the intrinsic electrical conductivity of semiconducting TMDs; (2) defect engineering can provide more active adsorption sites and decrease the length of the ion diffusion pathway; (3) the interlayer spacing expansion strategy is beneficial for reducing the diffusion energy barriers for metal ions in TMDs; (4) heteroatom doping

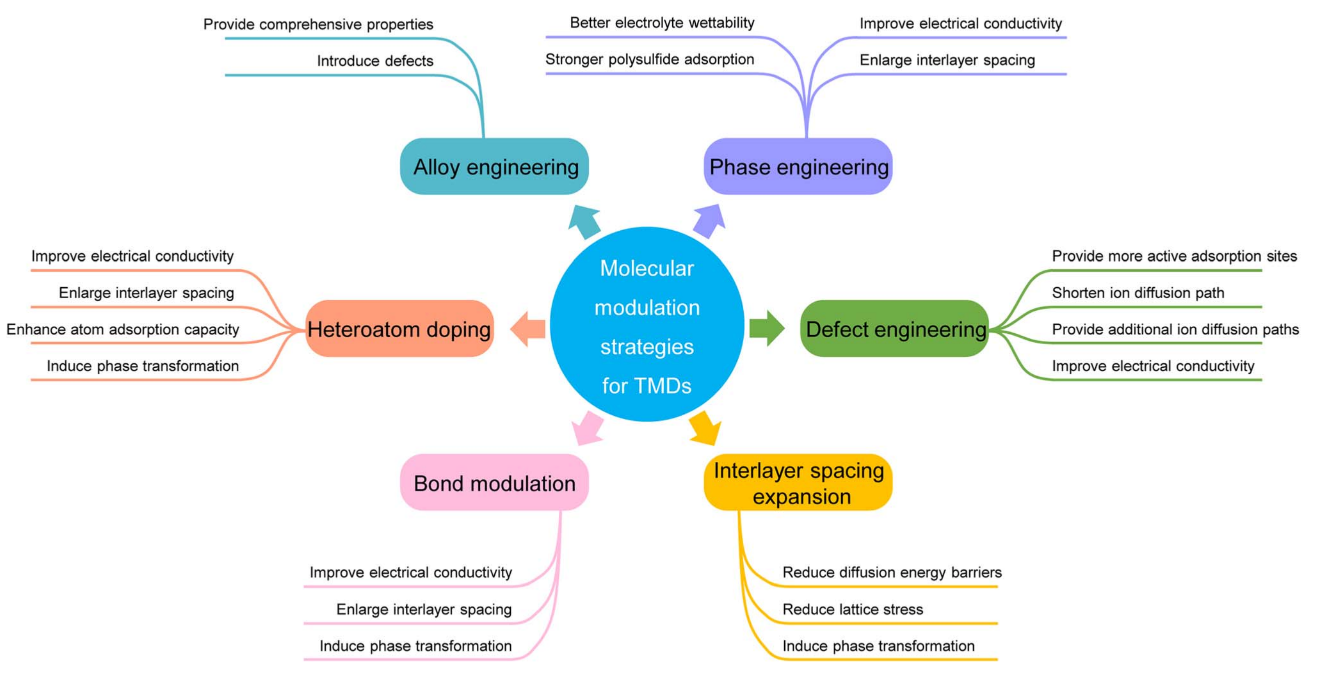


Fig. 12 A schematic summarizing the influences of different molecular modulation strategies on the properties of TMDs.

Open Access Article. Published on 19 janvris 2024. Downloaded on 23.02.2025 18:44:43.
This article is licensed under a Creative Commons Attribution-NonCommercial 3.0 Unported Licence.

is expected to improve the electrical conductivity and the atom adsorption capacity of TMDs; (5) alloy engineering is used to obtain comprehensive properties of TMDs; (6) bond modulation can enhance the electrical conductivity and the ion diffusion dynamics of TMDs. In addition to the main effects mentioned above, some extra advantages of molecular modulation strategies toward specific applications are also summarized (Fig. 12).

Although many advances have been achieved in developing TMD electrodes, much effort is still needed to further promote the development of TMDs as electrode materials from a molecular modulation viewpoint. (1) The conversion reaction provides high discharge capacity for some TMD electrodes, while the reversibility of the conversion reaction is not satisfactory. Although it has been reported that the dynamic properties of TMDs influence the reversibility of the conversion reaction, $VX_2$ compounds with excellent dynamic properties only exhibit a partially reversible conversion reaction. Therefore, extensive theoretical and experimental research on the dynamic properties of the conversion reaction at the molecular and atomic level is needed to make it fully reversible, which is crucial for employing TMDs in metal-ion batteries. (2) The precise modulation methods for TMD molecules are necessary to be developed, which only exist in the theoretical models currently. By manipulating TMD molecules precisely, the specific mechanisms and effects of various molecular modulation strategies can be better understood. In addition, the properties of TMDs can be flexibly adjusted to meet different needs, which is beneficial for providing more potential opportunities and leveraging the maximum advantages of TMDs. (3) Deeper theoretical calculations need to be performed to help understand the reaction mechanisms of TMDs and direct the experimental designs. Currently, most theoretical calculations focus on the level of single-layer or double-layer TMDs, which is very different from the actual situation. Therefore, many conclusions drawn from calculations are inconsistent with the experimental data, and the real mechanisms cannot be verified. (4) In the future, various *in situ* characterization techniques which can reveal the basic reaction mechanisms of TMDs before and after molecular modulation need to be developed. Despite significant progress in research on TMDs in recent years, there are still a large number of problems which need to be solved. By developing advanced *in situ* characterization techniques, many problems can be understood and solved from the source, which is helpful for developing practice and high-performance TMD electrodes with balanced and optimized properties.

## Author contributions

B. L. and J. Z. designed the scope of the paper. M. G. surveyed the relevant literature, and all authors wrote the paper.

## Conflicts of interest

There are no conflicts to declare.

## Acknowledgements

B. L. acknowledges financial support from the National Natural Science Foundation of China no. U20A20247 and 51922038. M. G. acknowledges financial support from the Postgraduate Scientific Research Innovation Project of Hunan Province no. CX20230407. A. M. R. acknowledges financial support through Clemson University's R. A. Bowen Fellowship funds.

## References

1 M. Armand and J. M. Tarascon, Building better batteries, *Nature*, 2008, **451**, 652–657.

2 Z. Zhu, T. Jiang, M. Ali, Y. Meng, Y. Jin, Y. Cui and W. Chen, Rechargeable Batteries for Grid Scale Energy Storage, *Chem. Rev.*, 2022, **122**, 16610–16751.

3 K. Chen, X. Shen, L. Luo, H. Chen, R. Cao, X. Feng, W. Chen, Y. Fang and Y. Cao, Correlating the Solvating Power of Solvents with the Strength of Ion-Dipole Interaction in Electrolytes of Lithium-ion Batteries, *Angew. Chem., Int. Ed.*, 2023, **62**, e202312373.

4 Y. Li, F. Wu, Y. Li, M. Liu, X. Feng, Y. Bai and C. Wu, Ether-based electrolytes for sodium ion batteries, *Chem. Soc. Rev.*, 2022, **51**, 4484–4536.

5 R. Usiskin, Y. Lu, J. Popovic, M. Law, P. Balaya, Y.-S. Hu and J. Maier, Fundamentals, status and promise of sodium-based batteries, *Nat. Rev. Mater.*, 2021, **6**, 1020–1035.

6 K. Chayambuka, G. Mulder, D. L. Danilov and P. H. L. Notten, From Li-Ion Batteries toward Na-Ion Chemistries: Challenges and Opportunities, *Adv. Energy Mater.*, 2020, **10**, 2001310.

7 Y. Feng, Y. Lv, H. Fu, M. Parekh, A. M. Rao, H. Wang, X. Tai, X. Yi, Y. Lin, J. Zhou and B. Lu, Co-activation for enhanced K-ion storage in battery anodes, *Natl. Sci. Rev.*, 2023, **10**, nwad118.

8 M. Gu, A. M. Rao, J. Zhou and B. Lu, In situ formed uniform and elastic SEI for high-performance batteries, *Energy Environ. Sci.*, 2023, **16**, 1166–1175.

9 H. Ding, J. Wang, J. Zhou, C. Wang and B. Lu, Building electrode skins for ultra-stable potassium metal batteries, *Nat. Commun.*, 2023, **14**, 2305.

10 Y. Liu, Y. Shi, C. Gao, Z. Shi, H. Ding, Y. Feng, Y. He, J. Sha, J. Zhou and B. Lu, Low-Temperature Potassium Batteries Enabled by Electric and Thermal Field Regulation, *Angew. Chem., Int. Ed.*, 2023, **62**, e202300016.

11 G. Fang, J. Zhou, A. Pan and S. Liang, Recent Advances in Aqueous Zinc-Ion Batteries, *ACS Energy Lett.*, 2018, **3**, 2480–2501.

12 C. Liu, X. Xie, B. Lu, J. Zhou and S. Liang, Electrolyte Strategies toward Better Zinc-Ion Batteries, *ACS Energy Lett.*, 2021, **6**, 1015–1033.

13 N. Zhang, X. Chen, M. Yu, Z. Niu, F. Cheng and J. Chen, Materials chemistry for rechargeable zinc-ion batteries, *Chem. Soc. Rev.*, 2020, **49**, 4203–4219.

14 B. Chen, D. Chao, E. Liu, M. Jaroniec, N. Zhao and S.-Z. Qiao, Transition metal dichalcogenides for alkali

 © 2024 The Author(s). Published by the Royal Society of Chemistry

Open Access Article. Published on 19 janvris 2024. Downloaded on 23.02.2025 18:44:43.
This article is licensed under a Creative Commons Attribution-NonCommercial 3.0 Unported Licence.

metal ion batteries: engineering strategies at the atomic level, *Energy Environ. Sci.*, 2020, **13**, 1096–1131.

15 H. Shuai, R. Liu, W. Li, X. Yang, H. Lu, Y. Gao, J. Xu and K. Huang, Recent Advances of Transition Metal Sulfides/Selenides Cathodes for Aqueous Zinc-Ion Batteries, *Adv. Energy Mater.*, 2023, **13**, 2202992.

16 L. Wang, Q. Zhang, J. Zhu, X. Duan, Z. Xu, Y. Liu, H. Yang and B. Lu, Nature of extra capacity in $MoS_2$ electrodes: molybdenum atoms accommodate with lithium, *Energy Storage Mater.*, 2019, **16**, 37–45.

17 M. S. Whittingham, Electrical Energy Storage and Intercalation Chemistry, *Science*, 1976, **192**, 1126–1127.

18 T. Wang, S. Chen, H. Pang, H. Xue and Y. Yu, $MoS_2$-Based Nanocomposites for Electrochemical Energy Storage, *Adv. Sci.*, 2017, **4**, 1600289.

19 X. Ren, Q. Zhao, W. D. McCulloch and Y. Wu, $MoS_2$ as a long-life host material for potassium ion intercalation, *Nano Res.*, 2017, **10**, 1313–1321.

20 W. S. V. Lee, T. Xiong, X. Wang and J. Xue, Unraveling $MoS_2$ and Transition Metal Dichalcogenides as Functional Zinc-Ion Battery Cathode: A Perspective, *Small Methods*, 2021, **5**, 2000815.

21 Y. Li, M. Wang and J. Sun, Molecular Engineering Strategies toward Molybdenum Diselenide Design for Energy Storage and Conversion, *Adv. Energy Mater.*, 2022, **12**, 2202600.

22 Q. Yun, L. Li, Z. Hu, Q. Lu, B. Chen and H. Zhang, Layered Transition Metal Dichalcogenide-Based Nanomaterials for Electrochemical Energy Storage, *Adv. Mater.*, 2020, **32**, 1903826.

23 L. Zhang, H. B. Wu, Y. Yan, X. Wang and X. W. Lou, Hierarchical $MoS_2$ microboxes constructed by nanosheets with enhanced electrochemical properties for lithium storage and water splitting, *Energy Environ. Sci.*, 2014, **7**, 3302–3306.

24 Y. Wang, W. Kang, X. Pu, Y. Liang, B. Xu, X. Lu, D. Sun and Y. Cao, Template-directed synthesis of $Co_2P/MoSe_2$ in a N-doped carbon hollow structure for efficient and stable sodium/potassium ion storage, *Nano Energy*, 2022, **93**, 106897.

25 B. Jia, Q. Yu, Y. Zhao, M. Qin, W. Wang, Z. Liu, C.-Y. Lao, Y. Liu, H. Wu, Z. Zhang and X. Qu, Bamboo-Like Hollow Tubes with $MoS_2$/N-Doped-C Interfaces Boost Potassium-Ion Storage, *Adv. Funct. Mater.*, 2018, **28**, 1803409.

26 S. Wang, Y. Si, P. Wan, S. Zhu, W. Chu and Z. Yu, $MoSe_2$ nanoflowers grown on 3D carbon network as an advanced anode for lithium ion batteries, *Mater. Lett.*, 2022, **310**, 131487.

27 M. Hong, J. Li, W. Zhang, S. Liu and H. Chang, Semimetallic 1T′ $WTe_2$ Nanorods as Anode Material for the Sodium Ion Battery, *Energy Fuels*, 2018, **32**, 6371–6377.

28 J. Ge, L. Fan, J. Wang, Q. Zhang, Z. Liu, E. Zhang, Q. Liu, X. Yu and B. Lu, $MoSe_2$/N-Doped Carbon as Anodes for Potassium-Ion Batteries, *Adv. Energy Mater.*, 2018, **8**, 1801477.

29 D. Sun, D. Ye, P. Liu, Y. Tang, J. Guo, L. Wang and H. Wang, $MoS_2$/Graphene Nanosheets from Commercial Bulky $MoS_2$ and Graphite as Anode Materials for High Rate Sodium-Ion Batteries, *Adv. Energy Mater.*, 2018, **8**, 1702383.

30 S. H. Choi, Y. N. Ko, J.-K. Lee and Y. C. Kang, 3D $MoS_2$–Graphene Microspheres Consisting of Multiple Nanospheres with Superior Sodium Ion Storage Properties, *Adv. Funct. Mater.*, 2015, **25**, 1780–1788.

31 J. Bai, B. Zhao, J. Zhou, J. Si, Z. Fang, K. Li, H. Ma, J. Dai, X. Zhu and Y. Sun, Glucose-Induced Synthesis of 1T-$MoS_2$/C Hybrid for High-Rate Lithium-Ion Batteries, *Small*, 2019, **15**, 1805420.

32 Y. Zhou, Y. Liu, M. Zhang, Q. Han, Y. Wang, X. Sun, X. Zhang, C. Dong, J. Sun, Z. Tang and F. Jiang, Rationally designed hierarchical N, P co-doped carbon connected 1T/2H-$MoS_2$ heterostructures with cooperative effect as ultrafast and durable anode materials for efficient sodium storage, *Chem. Eng. J.*, 2022, **433**, 133778.

33 W. Ding, L. Hu, J. Dai, X. Tang, R. Wei, Z. Sheng, C. Liang, D. Shao, W. Song, Q. Liu, M. Chen, X. Zhu, S. Chou, X. Zhu, Q. Chen, Y. Sun and S. X. Dou, Highly Ambient-Stable 1T-$MoS_2$ and 1T-$WS_2$ by Hydrothermal Synthesis under High Magnetic Fields, *ACS Nano*, 2019, **13**, 1694–1702.

34 D. Sun, D. Huang, H. Wang, G.-L. Xu, X. Zhang, R. Zhang, Y. Tang, D. Abd Ei-Hady, W. Alshitari, A. Saad Al-Bogami, K. Amine and M. Shao, 1T $MoS_2$ nanosheets with extraordinary sodium storage properties via thermal-driven ion intercalation assisted exfoliation of bulky $MoS_2$, *Nano Energy*, 2019, **61**, 361–369.

35 H. He, X. Li, D. Huang, J. Luan, S. Liu, W. K. Pang, D. Sun, Y. Tang, W. Zhou, L. He, C. Zhang, H. Wang and Z. Guo, Electron-Injection-Engineering Induced Phase Transition toward Stabilized 1T-$MoS_2$ with Extraordinary Sodium Storage Performance, *ACS Nano*, 2021, **15**, 8896–8906.

36 Y. Li, X. Dong, Z. Xu, M. Wang, R. Wang, J. Xie, Y. Ding, P. Su, C. Jiang, X. Zhang, L. Wei, J.-F. Li, Z. Chu, J. Sun and C. Huang, Piezoelectric 1T Phase $MoSe_2$ Nanoflowers and Crystallographically Textured Electrodes for Enhanced Low-Temperature Zinc-Ion Storage, *Adv. Mater.*, 2023, **35**, 2208615.

37 H. Fan, P. Mao, G. Lan, C. Liu, J. Chen, Z. Wang, Z. Li, R. Zheng, Y. Liu and H. Sun, Ultrathin Metallic-Phase Molybdenum Disulfide Nanosheets Stabilized on Functionalized Carbon Nanotubes Via Covalent Interface Interaction for Sodium- and Lithium-Ion Storage, *ACS Appl. Energy Mater.*, 2021, **4**, 9440–9449.

38 B. Chen, H. Lu, N. Zhao, C. Shi, E. Liu, C. He and L. Ma, Facile synthesis and electrochemical properties of continuous porous spheres assembled from defect-rich, interlayer-expanded, and few-layered $MoS_2$/C nanosheets for reversible lithium storage, *J. Power Sources*, 2018, **387**, 16–23.

39 Z. Lei, J. Zheng, X. He, Y. Wang, X. Yang, F. Xiao, H. Xue, P. Xiong, M. Wei, Q. Chen, Q. Qian and L. Zeng, Defect-rich $WS_2$–SPAN nanofibers for sodium/potassium-ion batteries: ultralong lifespans and wide-temperature workability, *Inorg. Chem. Front.*, 2023, **10**, 1187–1196.

40 K. Yao, Z. Xu, J. Huang, M. Ma, L. Fu, X. Shen, J. Li and M. Fu, Bundled Defect-Rich $MoS_2$ for a High-Rate and

Open Access Article. Published on 19 janvris 2024. Downloaded on 23.02.2025 18:44:43.
This article is licensed under a Creative Commons Attribution-NonCommercial 3.0 Unported Licence.

Long-Life Sodium-Ion Battery: Achieving 3D Diffusion of Sodium Ion by Vacancies to Improve Kinetics, *Small*, 2019, **15**, 1805405.

41 J. Liang, Z. Wei, C. Wang and J. Ma, Vacancy-induced sodium-ion storage in N-doped carbon Nanofiber@$MoS_2$ nanosheet arrays, *Electrochim. Acta*, 2018, **285**, 301–308.

42 D. Sha, Y. You, R. Hu, X. Cao, Y. Wei, H. Zhang, L. Pan and Z. Sun, Comprehensively Understanding the Role of Anion Vacancies on K-Ion Storage: A Case Study of Se-Vacancy-Engineered $VSe_2$, *Adv. Mater.*, 2023, **35**, 2211311.

43 Q. Zhu, W. Li, J. Wu, N. Tian, Y. Li, J. Yang, B. Liu and J. Jiang, Vacancy engineering in $WS_2$ nanosheets for enhanced potassium-ion storage, *J. Power Sources*, 2022, **542**, 231791.

44 W. Xu, C. Sun, K. Zhao, X. Cheng, S. Rawal, Y. Xu and Y. Wang, Defect engineering activating (boosting) zinc storage capacity of $MoS_2$, *Energy Storage Mater.*, 2019, **16**, 527–534.

45 Y. Bai, H. Zhang, B. Xiang, X. Liang, J. Hao, C. Zhu and L. Yan, Selenium Defect Boosted Electrochemical Performance of Binder-Free $VSe_2$ Nanosheets for Aqueous Zinc-Ion Batteries, *ACS Appl. Mater. Interfaces*, 2021, **13**, 23230–23238.

46 H. Wang, H. Jiang, Y. Hu, N. Li, X. Zhao and C. Li, 2D $MoS_2$/polyaniline heterostructures with enlarged interlayer spacing for superior lithium and sodium storage, *J. Mater. Chem. A*, 2017, **5**, 5383–5389.

47 L. Xing, K. Han, Q. Liu, Z. Liu, J. Chu, L. Zhang, X. Ma, Y. Bao, P. Li and W. Wang, Hierarchical two-atom-layered $WSe_2$/C ultrathin crumpled nanosheets assemblies: engineering the interlayer spacing boosts potassium-ion storage, *Energy Storage Mater.*, 2021, **36**, 309–317.

48 S. Di, P. Ding, Y. Wang, Y. Wu, J. Deng, L. Jia and Y. Li, Interlayer-expanded $MoS_2$ assemblies for enhanced electrochemical storage of potassium ions, *Nano Res.*, 2020, **13**, 225–230.

49 M. Huang, Y. Mai, L. Zhao, X. Liang, Z. Fang and X. Jie, Tuning the kinetics of zinc ion in $MoS_2$ by polyaniline intercalation, *Electrochim. Acta*, 2021, **388**, 138624.

50 Y.-R. Liu, Z.-W. Lei, R.-P. Liu, X.-Y. Li, P.-X. Xiong, Y.-J. Luo, Q.-H. Chen, M.-D. Wei, L.-X. Zeng and Q.-R. Qian, Sn-doped induced stable 1T-$WSe_2$ nanosheets entrenched on N-doped carbon with extraordinary half/full sodium/potassium storage performance, *Rare Met.*, 2023, **42**, 1557–1569.

51 Y. Zhang, H. Tao, T. Li, S. Du, J. Li, Y. Zhang and X. Yang, Vertically Oxygen-Incorporated $MoS_2$ Nanosheets Coated on Carbon Fibers for Sodium-Ion Batteries, *ACS Appl. Mater. Interfaces*, 2018, **10**, 35206–35215.

52 S. Li, Y. Liu, X. Zhao, K. Cui, Q. Shen, P. Li, X. Qu and L. Jiao, Molecular Engineering on $MoS_2$ Enables Large Interlayers and Unlocked Basal Planes for High-Performance Aqueous Zn-Ion Storage, *Angew. Chem., Int. Ed.*, 2021, **60**, 20286–20293.

53 J. Li, H. Yan, W. Wei and L. Meng, Microwave-assisted mass synthesis of $Mo_{1-x}W_xS_2$ alloy composites with a tunable lithium storage property, *Dalton Trans.*, 2018, **47**, 15148–15154.

54 H.-N. Fan, X.-Y. Wang, H.-B. Yu, Q.-F. Gu, S.-L. Chen, Z. Liu, X.-H. Chen, W.-B. Luo and H.-K. Liu, Enhanced Potassium Ion Battery by Inducing Interlayer Anionic Ligands in $MoS_{1.5}Se_{0.5}$ Nanosheets with Exploration of the Mechanism, *Adv. Energy Mater.*, 2020, **10**, 1904162.

55 H. He, D. Huang, Q. Gan, J. Hao, S. Liu, Z. Wu, W. K. Pang, B. Johannessen, Y. Tang, J.-L. Luo, H. Wang and Z. Guo, Anion Vacancies Regulating Endows MoSSe with Fast and Stable Potassium Ion Storage, *ACS Nano*, 2019, **13**, 11843–11852.

56 H. Li, B. Chen, R. Gao, F. Xu, X. Wen, X. Zhong, C. Li, Z. Piao, N. Hu, X. Xiao, F. Shao, G. Zhou and J. Yang, Integrating molybdenum sulfide selenide-based cathode with C-O-Mo heterointerface design and atomic engineering for superior aqueous Zn-ion batteries, *Nano Res.*, 2023, **16**, 4933–4940.

57 S. Zhang, G. Wang, J. Jin, L. Zhang, Z. Wen and J. Yang, Robust and Conductive Red $MoSe_2$ for Stable and Fast Lithium Storage, *ACS Nano*, 2018, **12**, 4010–4018.

58 T. Lei, M. Gu, H. Fu, J. Wang, L. Wang, J. Zhou, H. Liu and B. Lu, Bond modulation of $MoSe_{2+x}$ driving combined intercalation and conversion reactions for high-performance K cathodes, *Chem. Sci.*, 2023, **14**, 2528–2536.

59 M. Chhowalla, H. S. Shin, G. Eda, L.-J. Li, K. P. Loh and H. Zhang, The chemistry of two-dimensional layered transition metal dichalcogenide nanosheets, *Nat. Chem.*, 2013, **5**, 263–275.

60 X. Qian, J. Liu, L. Fu and J. Li, Quantum spin Hall effect in two-dimensional transition metal dichalcogenides, *Science*, 2014, **346**, 1344–1347.

61 Q. H. Wang, K. Kalantar-Zadeh, A. Kis, J. N. Coleman and M. S. Strano, Electronics and optoelectronics of two-dimensional transition metal dichalcogenides, *Nat. Nanotechnol.*, 2012, **7**, 699–712.

62 D. Voiry, A. Mohite and M. Chhowalla, Phase engineering of transition metal dichalcogenides, *Chem. Soc. Rev.*, 2015, **44**, 2702–2712.

63 I. Song, C. Park and H. C. Choi, Synthesis and properties of molybdenum disulphide: from bulk to atomic layers, *RSC Adv.*, 2015, **5**, 7495–7514.

64 S. Jayabal, J. Wu, J. Chen, D. Geng and X. Meng, Metallic 1T-$MoS_2$ nanosheets and their composite materials: Preparation, properties and emerging applications, *Mater. Today Energy*, 2018, **10**, 264–279.

65 J. Strachan, A. F. Masters and T. Maschmeyer, 3R-$MoS_2$ in Review: History, Status, and Outlook, *ACS Appl. Energy Mater.*, 2021, **4**, 7405–7418.

66 A. Kumar and P. K. Ahluwalia, A first principle Comparative study of electronic and optical properties of 1H – $MoS_2$ and 2H – $MoS_2$, *Mater. Chem. Phys.*, 2012, **135**, 755–761.

67 Y. S. Huang, Preparation, Electrical and Modulation Optical Properties of 2H-MoSe2, *Chin. J. Phys.*, 1984, **22**, 43–53.

68 S. Zhao, T. Hotta, T. Koretsune, K. Watanabe, T. Taniguchi, K. Sugawara, T. Takahashi, H. Shinohara and R. Kitaura, Two-dimensional metallic $NbS_2$: growth, optical


© 2024 The Author(s). Published by the Royal Society of Chemistry

Open Access Article. Published on 19 janvris 2024. Downloaded on 23.02.2025 18:44:43.
This article is licensed under a Creative Commons Attribution-NonCommercial 3.0 Unported Licence.

identification and transport properties, *2D Mater.*, 2016, **3**, 025027.
69 J. Feng, X. Sun, C. Wu, L. Peng, C. Lin, S. Hu, J. Yang and Y. Xie, Metallic Few-Layered $VS_2$ Ultrathin Nanosheets: High Two-Dimensional Conductivity for In-Plane Supercapacitors, *J. Am. Chem. Soc.*, 2011, **133**, 17832–17838.
70 W. Choi, N. Choudhary, G. H. Han, J. Park, D. Akinwande and Y. H. Lee, Recent development of two-dimensional transition metal dichalcogenides and their applications, *Mater. Today*, 2017, **20**, 116–130.
71 J. Li, B. Zhao, P. Chen, R. Wu, B. Li, Q. Xia, G. Guo, J. Luo, K. Zang, Z. Zhang, H. Ma, G. Sun, X. Duan and X. Duan, Synthesis of Ultrathin Metallic $MTe_2$ (M = V, Nb, Ta) Single-Crystalline Nanoplates, *Adv. Mater.*, 2018, **30**, 1801043.
72 H. Liu, Y. Xue, J.-A. Shi, R. A. Guzman, P. Zhang, Z. Zhou, Y. He, C. Bian, L. Wu, R. Ma, J. Chen, J. Yan, H. Yang, C.-M. Shen, W. Zhou, L. Bao and H.-J. Gao, Observation of the Kondo Effect in Multilayer Single-Crystalline $VTe_2$ Nanoplates, *Nano Lett.*, 2019, **19**, 8572–8580.
73 C. Zhu, D. Gao, J. Ding, D. Chao and J. Wang, TMD-based highly efficient electrocatalysts developed by combined computational and experimental approaches, *Chem. Soc. Rev.*, 2018, **47**, 4332–4356.
74 E. Torun, H. Sahin, S. Cahangirov, A. Rubio and F. M. Peeters, Anisotropic electronic, mechanical, and optical properties of monolayer $WTe_2$, *J. Appl. Phys.*, 2016, **119**, 074307.
75 M. Rahman, K. Davey and S.-Z. Qiao, Advent of 2D Rhenium Disulfide ($ReS_2$): Fundamentals to Applications, *Adv. Funct. Mater.*, 2017, **27**, 1606129.
76 H.-X. Zhong, S. Gao, J.-J. Shi and L. Yang, Quasiparticle band gaps, excitonic effects, and anisotropic optical properties of the monolayer distorted 1T diamond-chain structures $ReS_2$ and $ReSe_2$, *Phys. Rev. B: Condens. Matter Mater. Phys.*, 2015, **92**, 115438.
77 J. A. Wilson and A. D. Yoffe, The transition metal dichalcogenides discussion and interpretation of the observed optical, electrical and structural properties, *Adv. Phys.*, 1969, **18**, 193–335.
78 L. Peng, Y. Zhu, D. Chen, R. S. Ruoff and G. Yu, Two-Dimensional Materials for Beyond-Lithium-Ion Batteries, *Adv. Energy Mater.*, 2016, **6**, 1600025.
79 S. Hao, X. Shen, M. Tian, R. Yu, Z. Wang and L. Chen, Reversible conversion of $MoS_2$ upon sodium extraction, *Nano Energy*, 2017, **41**, 217–224.
80 X. Fang, C. Hua, X. Guo, Y. Hu, Z. Wang, X. Gao, F. Wu, J. Wang and L. Chen, Lithium storage in commercial $MoS_2$ in different potential ranges, *Electrochim. Acta*, 2012, **81**, 155–160.
81 T. Zhao, H. Shu, Z. Shen, H. Hu, J. Wang and X. Chen, Electrochemical Lithiation Mechanism of Two-Dimensional Transition-Metal Dichalcogenide Anode Materials: Intercalation versus Conversion Reactions, *J. Phys. Chem. C*, 2019, **123**, 2139–2146.
82 L. Zhang, D. Sun, J. Kang, J. Feng, H. A. Bechtel, L.-W. Wang, E. J. Cairns and J. Guo, Electrochemical Reaction Mechanism of the $MoS_2$ Electrode in a Lithium-Ion Cell Revealed by in Situ and Operando X-ray Absorption Spectroscopy, *Nano Lett.*, 2018, **18**, 1466–1475.
83 J. Zhou, L. Wang, M. Yang, J. Wu, F. Chen, W. Huang, N. Han, H. Ye, F. Zhao, Y. Li and Y. Li, Hierarchical $VS_2$ Nanosheet Assemblies: A Universal Host Material for the Reversible Storage of Alkali Metal Ions, *Adv. Mater.*, 2017, **29**, 1702061.
84 L. Zhang, D. Sun, Q. Wei, H. Ju, J. Feng, J. Zhu, L. Mai, E. J. Cairns and J. Guo, Understanding the electrochemical reaction mechanism of $VS_2$ nanosheets in lithium-ion cells by multiple in situ and ex situ x-ray spectroscopy, *J. Phys. D: Appl. Phys.*, 2018, **51**, 494001.
85 C. Yang, J. Feng, F. Lv, J. Zhou, C. Lin, K. Wang, Y. Zhang, Y. Yang, W. Wang, J. Li and S. Guo, Metallic Graphene-Like $VSe_2$ Ultrathin Nanosheets: Superior Potassium-Ion Storage and Their Working Mechanism, *Adv. Mater.*, 2018, **30**, 1800036.
86 G. Wang, Y. Zhang, H. S. Cho, X. Zhao, F. Kim and J. Zou, Revisiting the Structural Evolution of $MoS_2$ During Alkali Metal (Li, Na, and K) Intercalation, *ACS Appl. Energy Mater.*, 2021, **4**, 14180–14190.
87 V. P. H. Huy, Y. N. Ahn and J. Hur, Recent Advances in Transition Metal Dichalcogenide Cathode Materials for Aqueous Rechargeable Multivalent Metal-Ion Batteries, *Nanomaterials*, 2021, **11**, 1517.
88 K. Yao, Z. Xu, M. Ma, J. Li, F. Lu and J. Huang, Densified Metallic $MoS_2$/Graphene Enabling Fast Potassium-Ion Storage with Superior Gravimetric and Volumetric Capacities, *Adv. Funct. Mater.*, 2020, **30**, 2001484.
89 S. Yan, W. Qiao, X. He, X. Guo, L. Xi, W. Zhong and Y. Du, Enhancement of magnetism by structural phase transition in $MoS_2$, *Appl. Phys. Lett.*, 2015, **106**, 012408.
90 T. Xiang, S. Tao, W. Xu, Q. Fang, C. Wu, D. Liu, Y. Zhou, A. Khalil, Z. Muhammad, W. Chu, Z. Wang, H. Xiang, Q. Liu and L. Song, Stable 1T-$MoSe_2$ and Carbon Nanotube Hybridized Flexible Film: Binder-Free and High-Performance Li-Ion Anode, *ACS Nano*, 2017, **11**, 6483–6491.
91 K. Wu, X. Cao, M. Li, B. Lei, J. Zhan and M. Wu, Bottom-Up Synthesis of $MoS_2$/CNTs Hollow Polyhedron with 1T/2H Hybrid Phase for Superior Potassium-Ion Storage, *Small*, 2020, **16**, 2004178.
92 M. Srinivaas, C.-Y. Wu, J.-G. Duh and J. M. Wu, Highly Rich 1T Metallic Phase of Few-Layered $WS_2$ Nanoflowers for Enhanced Storage of Lithium-Ion Batteries, *ACS Sustain. Chem. Eng.*, 2019, **7**, 10363–10370.
93 M. Acerce, D. Voiry and M. Chhowalla, Metallic 1T phase $MoS_2$ nanosheets as supercapacitor electrode materials, *Nat. Nanotechnol.*, 2015, **10**, 313–318.
94 L. Liu, W. Yang, H. Chen, X. Chen, K. Zhang, Q. Zeng, S. Lei, J. Huang, S. Li and S. Peng, High zinc-ion intercalation reaction activity of $MoS_2$ cathode based on regulation of thermodynamic metastability and interlayer water, *Electrochim. Acta*, 2022, **410**, 140016.

© 2024 The Author(s). Published by the Royal Society of Chemistry

Open Access Article. Published on 19 janvris 2024. Downloaded on 23.02.2025 18:44:43.
This article is licensed under a Creative Commons Attribution-NonCommercial 3.0 Unported Licence.


95 Y. Liu and X. Wu, Recent Advances of Transition Metal Chalcogenides as Cathode Materials for Aqueous Zinc-Ion Batteries, *Nanomaterials*, 2022, **12**, 3298.

96 J. He, G. Hartmann, M. Lee, G. S. Hwang, Y. Chen and A. Manthiram, Freestanding 1T $MoS_2$/graphene heterostructures as a highly efficient electrocatalyst for lithium polysulfides in Li–S batteries, *Energy Environ. Sci.*, 2019, **12**, 344–350.

97 J. Liu, N. Gong, W. Peng, Y. Li, F. Zhang and X. Fan, Vertically aligned 1 T phase $MoS_2$ nanosheet array for high-performance rechargeable aqueous Zn-ion batteries, *Chem. Eng. J.*, 2022, **428**, 130981.

98 J. Liu, P. Xu, J. Liang, H. Liu, W. Peng, Y. Li, F. Zhang and X. Fan, Boosting aqueous zinc-ion storage in $MoS_2$ via controllable phase, *Chem. Eng. J.*, 2020, **389**, 124405.

99 W.-H. Ryu, J.-W. Jung, K. Park, S.-J. Kim and I.-D. Kim, Vine-like $MoS_2$ anode materials self-assembled from 1-D nanofibers for high capacity sodium rechargeable batteries, *Nanoscale*, 2014, **6**, 10975–10981.

100 B. Yu, Y. Chen, Z. Wang, D. Chen, X. Wang, W. Zhang, J. He and W. He, 1T-$MoS_2$ nanotubes wrapped with N-doped graphene as highly-efficient absorbent and electrocatalyst for Li–S batteries, *J. Power Sources*, 2020, **447**, 227364.

101 M. Wang, L. Fan, D. Tian, X. Wu, Y. Qiu, C. Zhao, B. Guan, Y. Wang, N. Zhang and K. Sun, Rational Design of Hierarchical $SnO_2$/1T-$MoS_2$ Nanoarray Electrode for Ultralong-Life Li–S Batteries, *ACS Energy Lett.*, 2018, **3**, 1627–1633.

102 H. Shu, F. Li, C. Hu, P. Liang, D. Cao and X. Chen, The capacity fading mechanism and improvement of cycling stability in $MoS_2$-based anode materials for lithium-ion batteries, *Nanoscale*, 2016, **8**, 2918–2926.

103 Y. Zhang, Z. Mu, C. Yang, Z. Xu, S. Zhang, X. Zhang, Y. Li, J. Lai, Z. Sun, Y. Yang, Y. Chao, C. Li, X. Ge, W. Yang and S. Guo, Rational Design of MXene/1T-2H $MoS_2$-C Nanohybrids for High-Performance Lithium–Sulfur Batteries, *Adv. Funct. Mater.*, 2018, **28**, 1707578.

104 Z. Lei, J. Zhan, L. Tang, Y. Zhang and Y. Wang, Recent Development of Metallic (1T) Phase of Molybdenum Disulfide for Energy Conversion and Storage, *Adv. Energy Mater.*, 2018, **8**, 1703482.

105 W.-j. Tang, X.-l. Wang, D. Xie, X.-h. Xia, C.-d. Gu and J.-p. Tu, Hollow metallic 1T $MoS_2$ arrays grown on carbon cloth: a freestanding electrode for sodium ion batteries, *J. Mater. Chem. A*, 2018, **6**, 18318–18324.

106 J. Wu, J. Liu, J. Cui, S. Yao, M. Ihsan-Ul-Haq, N. Mubarak, E. Quattrocchi, F. Ciucci and J.-K. Kim, Dual-phase $MoS_2$ as a high-performance sodium-ion battery anode, *J. Mater. Chem. A*, 2020, **8**, 2114–2122.

107 Z. Zhao, T. Xu and X. Yu, Unlock the Potassium Storage Behavior of Single-Phased Tungsten Selenide Nanorods via Large Cation Insertion, *Adv. Mater.*, 2023, **35**, 2208096.

108 F. Liu, Y. Zou, X. Tang, L. Mao, D. Du, H. Wang, M. Zhang, Z. Wang, N. Yao, W. Zhao, M. Bai, T. Zhao, Y. Liu and Y. Ma, Phase Engineering and Alkali Cation Stabilization for 1T Molybdenum Dichalcogenides Monolayers, *Adv. Funct. Mater.*, 2022, **32**, 2204601.

109 H. He, H. Zhang, D. Huang, W. Kuang, X. Li, J. Hao, Z. Guo and C. Zhang, Harnessing Plasma-Assisted Doping Engineering to Stabilize Metallic Phase MoSe2 for Fast and Durable Sodium-Ion Storage, *Adv. Mater.*, 2022, **34**, 2200397.

110 P. Li, Y. Yang, S. Gong, F. Lv, W. Wang, Y. Li, M. Luo, Y. Xing, Q. Wang and S. Guo, Co-doped 1T-$MoS_2$ nanosheets embedded in N, S-doped carbon nanobowls for high-rate and ultra-stable sodium-ion batteries, *Nano Res.*, 2019, **12**, 2218–2223.

111 P. Xiong, R. Ma, N. Sakai, L. Nurdiwijayanto and T. Sasaki, Unilamellar Metallic $MoS_2$/Graphene Superlattice for Efficient Sodium Storage and Hydrogen Evolution, *ACS Energy Lett.*, 2018, **3**, 997–1005.

112 Y. Fang, Y. Lv, F. Gong, A. A. Elzatahry, G. Zheng and D. Zhao, Synthesis of 2D-Mesoporous-Carbon/$MoS_2$ Heterostructures with Well-Defined Interfaces for High-Performance Lithium-Ion Batteries, *Adv. Mater.*, 2016, **28**, 9385–9390.

113 M. Jiang, Y. Hu, B. Mao, Y. Wang, Z. Yang, T. Meng, X. Wang and M. Cao, Strain-regulated Gibbs free energy enables reversible redox chemistry of chalcogenides for sodium ion batteries, *Nat. Commun.*, 2022, **13**, 5588.

114 X. Chia, A. Y. S. Eng, A. Ambrosi, S. M. Tan and M. Pumera, Electrochemistry of Nanostructured Layered Transition-Metal Dichalcogenides, *Chem. Rev.*, 2015, **115**, 11941–11966.

115 R. Zhou, H. Wang, J. Chang, C. Yu, H. Dai, Q. Chen, J. Zhou, H. Yu, G. Sun and W. Huang, Ammonium Intercalation Induced Expanded 1T-Rich Molybdenum Diselenides for Improved Lithium Ion Storage, *ACS Appl. Mater. Interfaces*, 2021, **13**, 17459–17466.

116 J. Yang, J. Wang, L. Zhu, X. Wang, X. Dong, W. Zeng, J. Wang and F. Pan, Boosting magnesium storage in $MoS_2$ via a 1T phase introduction and interlayer expansion strategy: theoretical prediction and experimental verification, *Sustain. Energy Fuels*, 2021, **5**, 5471–5480.

117 W. Zong, C. Yang, L. Mo, Y. Ouyang, H. Guo, L. Ge, Y.-E. Miao, D. Rao, J. Zhang, F. Lai and T. Liu, Elucidating dual-defect mechanism in rhenium disulfide nanosheets with multi-dimensional ion transport channels for ultrafast sodium storage, *Nano Energy*, 2020, **77**, 105189.

118 J. Mei, Y. Zhang, T. Liao, Z. Sun and S. X. Dou, Strategies for improving the lithium-storage performance of 2D nanomaterials, *Natl. Sci. Rev.*, 2018, **5**, 389–416.

119 Y. Zhao, D. Yang, T. He, J. Li, L. Wei, D. Wang, Y. Wang, X. Wang, G. Chen and Y. Wei, Vacancy engineering in $VS_2$ nanosheets for ultrafast pseudocapacitive sodium ion storage, *Chem. Eng. J.*, 2021, **421**, 129715.

120 T. Liu, N. Peng, X. Zhang, R. Zheng, M. Xia, H. Yu, M. Shui, Y. Xie and J. Shu, Controllable defect engineering enhanced bond strength for stable electrochemical energy storage, *Nano Energy*, 2021, **79**, 105460.

121 F. Liu and Z. Fan, Defect engineering of two-dimensional materials for advanced energy conversion and storage, *Chem. Soc. Rev.*, 2023, **52**, 1723–1772.


 © 2024 The Author(s). Published by the Royal Society of Chemistry

Open Access Article. Published on 19 janvris 2024. Downloaded on 23.02.2025 18:44:43.
This article is licensed under a Creative Commons Attribution-NonCommercial 3.0 Unported Licence.

122 Y. Jia, K. Jiang, H. Wang and X. Yao, The Role of Defect Sites in Nanomaterials for Electrocatalytic Energy Conversion, *Chem*, 2019, **5**, 1371–1397.
123 P. Gao, Z. Chen, Y. Gong, R. Zhang, H. Liu, P. Tang, X. Chen, S. Passerini and J. Liu, The Role of Cation Vacancies in Electrode Materials for Enhanced Electrochemical Energy Storage: Synthesis, Advanced Characterization, and Fundamentals, *Adv. Energy Mater.*, 2020, **10**, 1903780.
124 G. Barik and S. Pal, Defect Induced Performance Enhancement of Monolayer $MoS_2$ for Li- and Na-Ion Batteries, *J. Phys. Chem. C*, 2019, **123**, 21852–21865.
125 J. Kunstmann, T. B. Wendumu and G. Seifert, Localized defect states in $MoS_2$ monolayers: electronic and optical properties, *Phys. Status Solidi B*, 2017, **254**, 1600645.
126 Y. Li, R. Zhang, W. Zhou, X. Wu, H. Zhang and J. Zhang, Hierarchical $MoS_2$ Hollow Architectures with Abundant Mo Vacancies for Efficient Sodium Storage, *ACS Nano*, 2019, **13**, 5533–5540.
127 T. Liu, X. Zhang, M. Xia, H. Yu, N. Peng, C. Jiang, M. Shui, Y. Xie, T.-F. Yi and J. Shu, Functional cation defects engineering in $TiS_2$ for high-stability anode, *Nano Energy*, 2020, **67**, 104295.
128 J. Zhang, A. Yang, X. Wu, J. van de Groep, P. Tang, S. Li, B. Liu, F. Shi, J. Wan, Q. Li, Y. Sun, Z. Lu, X. Zheng, G. Zhou, C.-L. Wu, S.-C. Zhang, M. L. Brongersma, J. Li and Y. Cui, Reversible and selective ion intercalation through the top surface of few-layer $MoS_2$, *Nat. Commun.*, 2018, **9**, 5289.
129 Y. Liu, B. V. Merinov and W. A. Goddard, Origin of low sodium capacity in graphite and generally weak substrate binding of Na and Mg among alkali and alkaline earth metals, *Proc. Natl. Acad. Sci. U. S. A.*, 2016, **113**, 3735–3739.
130 F. Zhu, H. Zhang, Z. Lu, D. Kang and L. Han, Controlled defective engineering of $MoS_2$ nanosheets for rechargeable Mg batteries, *J. Energy Storage*, 2021, **42**, 103046.
131 Q. Zhang, S. Tan, R. G. Mendes, Z. Sun, Y. Chen, X. Kong, Y. Xue, M. H. Rümmeli, X. Wu, S. Chen and L. Fu, Extremely Weak van der Waals Coupling in Vertical $ReS_2$ Nanowalls for High-Current-Density Lithium-Ion Batteries, *Adv. Mater.*, 2016, **28**, 2616–2623.
132 S. Tongay, H. Sahin, C. Ko, A. Luce, W. Fan, K. Liu, J. Zhou, Y.-S. Huang, C.-H. Ho, J. Yan, D. F. Ogletree, S. Aloni, J. Ji, S. Li, J. Li, F. M. Peeters and J. Wu, Monolayer behaviour in bulk $ReS_2$ due to electronic and vibrational decoupling, *Nat. Commun.*, 2014, **5**, 3252.
133 J. Xu, J. Zhang, W. Zhang and C.-S. Lee, Interlayer Nanoarchitectonics of Two-Dimensional Transition-Metal Dichalcogenides Nanosheets for Energy Storage and Conversion Applications, *Adv. Energy Mater.*, 2017, **7**, 1700571.
134 L. Wu, M. Gu, Y. Feng, S. Chen, L. Fan, X. Yu, K. Guo, J. Zhou and B. Lu, Layered Superconductor $Cu_{0.11}TiSe_2$ as a High-Stable K-Cathode, *Adv. Funct. Mater.*, 2022, **32**, 2109893.
135 J. Shuai, H. D. Yoo, Y. Liang, Y. Li, Y. Yao and L. C. Grabow, Density functional theory study of Li, Na, and Mg intercalation and diffusion in $MoS_2$ with controlled interlayer spacing, *Mater. Res. Express*, 2016, **3**, 064001.
136 N. Zheng, G. Jiang, X. Chen, J. Mao, Y. Zhou and Y. Li, Rational design of a tubular, interlayer expanded $MoS_2$–N/O doped carbon composite for excellent potassium-ion storage, *J. Mater. Chem. A*, 2019, **7**, 9305–9315.
137 Y. Li, D. Wu, Z. Zhou, C. R. Cabrera and Z. Chen, Enhanced Li Adsorption and Diffusion on $MoS_2$ Zigzag Nanoribbons by Edge Effects: A Computational Study, *J. Phys. Chem. Lett.*, 2012, **3**, 2221–2227.
138 H. J. Chen, J. Huang, X. L. Lei, M. S. Wu, G. Liu, C. Y. Ouyang and B. Xu, Adsorption and Diffusion of Lithium on $MoS_2$ Monolayer: The Role of Strain and Concentration, *Int. J. Electrochem. Sci.*, 2013, **8**, 2196–2203.
139 H. Hwang, H. Kim and J. Cho, $MoS_2$ Nanoplates Consisting of Disordered Graphene-like Layers for High Rate Lithium Battery Anode Materials, *Nano Lett.*, 2011, **11**, 4826–4830.
140 H. Liu, D. Su, R. Zhou, B. Sun, G. Wang and S. Z. Qiao, Highly Ordered Mesoporous $MoS_2$ with Expanded Spacing of the (002) Crystal Plane for Ultrafast Lithium Ion Storage, *Adv. Energy Mater.*, 2012, **2**, 970–975.
141 K. Ma, Y. Liu, H. Jiang, Y. Hu, R. Si, H. Liu and C. Li, Multivalence-Ion Intercalation Enables Ultrahigh 1T Phase $MoS_2$ Nanoflowers to Enhanced Sodium-Storage Performance, *CCS Chem.*, 2020, **3**, 1472–1482.
142 G. Du, Z. Guo, S. Wang, R. Zeng, Z. Chen and H. Liu, Superior stability and high capacity of restacked molybdenum disulfide as anode material for lithium ion batteries, *Chem. Commun.*, 2010, **46**, 1106–1108.
143 E. Benavente, M. A. S. Ana, F. Mendizábal and G. González, Intercalation chemistry of molybdenum disulfide, *Coord. Chem. Rev.*, 2002, **224**, 87–109.
144 K. D. Rasamani, F. Alimohammadi and Y. Sun, Interlayer-expanded $MoS_2$, *Mater. Today*, 2017, **20**, 83–91.
145 W. M. R. Divigalpitiya, R. F. Frindt and S. R. Morrison, Inclusion Systems of Organic Molecules in Restacked Single-Layer Molybdenum Disulfide, *Science*, 1989, **246**, 369–371.
146 A. Zak, Y. Feldman, V. Lyakhovitskaya, G. Leitus, R. Popovitz-Biro, E. Wachtel, H. Cohen, S. Reich and R. Tenne, Alkali Metal Intercalated Fullerene-Like $MS_2$ (M = W, Mo) Nanoparticles and Their Properties, *J. Am. Chem. Soc.*, 2002, **124**, 4747–4758.
147 Z. Hu, L. Wang, K. Zhang, J. Wang, F. Cheng, Z. Tao and J. Chen, $MoS_2$ Nanoflowers with Expanded Interlayers as High-Performance Anodes for Sodium-Ion Batteries, *Angew. Chem., Int. Ed.*, 2014, **53**, 12794–12798.
148 G. González, M. A. S. Ana, E. Benavente, J. P. Donoso, T. J. Bonagamba, N. C. Mello and H. Panepucci, Electrical conductivity and lithium diffusion in molybdenum disulfide intercalated with poly(ethylene oxide), *Solid State Ionics*, 1996, **85**, 225–230.
149 W. Ye, F. Wu, N. Shi, H. Zhou, Q. Chi, W. Chen, S. Du, P. Gao, H. Li and S. Xiong, Metal–Semiconductor Phase Twinned Hierarchical $MoS_2$ Nanowires with Expanded

Open Access Article. Published on 19 janvris 2024. Downloaded on 23.02.2025 18:44:43. This article is licensed under a Creative Commons Attribution-NonCommercial 3.0 Unported Licence.

Interlayers for Sodium-Ion Batteries with Ultralong Cycle Life, *Small*, 2020, **16**, 1906607.

150 R. Bissessur and P. K. Y. Liu, Direct insertion of polypyrrole into molybdenum disulfide, *Solid State Ionics*, 2006, **177**, 191–196.

151 Y. Li, Y. Liang, F. C. R. Hernandez, H. D. Yoo, Q. An and Y. Yao, Enhancing sodium-ion battery performance with interlayer-expanded $MoS_2$–PEO nanocomposites, *Nano Energy*, 2015, **15**, 453–461.

152 K. Chang, W. Chen, L. Ma, H. Li, H. Li, F. Huang, Z. Xu, Q. Zhang and J.-Y. Lee, Graphene-like $MoS_2$/amorphous carbon composites with high capacity and excellent stability as anode materials for lithium ion batteries, *J. Mater. Chem.*, 2011, **21**, 6251–6257.

153 Y. Liu, X. Wang, X. Song, Y. Dong, L. Yang, L. Wang, D. Jia, Z. Zhao and J. Qiu, Interlayer expanded $MoS_2$ enabled by edge effect of graphene nanoribbons for high performance lithium and sodium ion batteries, *Carbon*, 2016, **109**, 461–471.

154 Y. Liu, Y. Yuan, L. Peng, L. Cheng, B. An, Y. Wang, Q. Wei, X. Xia and H. Zhou, Study on the construction of interlayer adjustable C@$MoS_2$ fiber anode by biomass confining and its lithium/sodium storage mechanism, *ChemSusChem*, 2023, e202300576.

155 H. Jiang, D. Ren, H. Wang, Y. Hu, S. Guo, H. Yuan, P. Hu, L. Zhang and C. Li, 2D Monolayer $MoS_2$–Carbon Interoverlapped Superstructure: Engineering Ideal Atomic Interface for Lithium Ion Storage, *Adv. Mater.*, 2015, **27**, 3687–3695.

156 N. Feng, R. Meng, L. Zu, Y. Feng, C. Peng, J. Huang, G. Liu, B. Chen and J. Yang, A polymer-direct-intercalation strategy for $MoS_2$/carbon-derived heteroaerogels with ultrahigh pseudocapacitance, *Nat. Commun.*, 2019, **10**, 1372.

157 H. Liang, Z. Cao, F. Ming, W. Zhang, D. H. Anjum, Y. Cui, L. Cavallo and H. N. Alshareef, Aqueous Zinc-Ion Storage in $MoS_2$ by Tuning the Intercalation Energy, *Nano Lett.*, 2019, **19**, 3199–3206.

158 P. Jing, H. Lu, W. Yang and Y. Cao, Interlayer-expanded and binder-free $VS_2$ nanosheets assemblies for enhanced $Mg^{2+}$ and $Li^+/Mg^{2+}$ hybrid ion storage, *Electrochim. Acta*, 2020, **330**, 135263.

159 M. Wang, H. Ye, V. Vasudevan and N. V. Medhekar, Enhancing kinetic and electrochemical performance of layered $MoS_2$ cathodes with interlayer expansion for Mg-ion batteries, *J. Power Sources*, 2022, **542**, 231722.

160 S. Li, Y. Liu, X. Zhao, Q. Shen, W. Zhao, Q. Tan, N. Zhang, P. Li, L. Jiao and X. Qu, Sandwich-Like Heterostructures of $MoS_2$/Graphene with Enlarged Interlayer Spacing and Enhanced Hydrophilicity as High-Performance Cathodes for Aqueous Zinc-Ion Batteries, *Adv. Mater.*, 2021, **33**, 2007480.

161 Y. Liang, H. D. Yoo, Y. Li, J. Shuai, H. A. Calderon, F. C. R. Hernandez, L. C. Grabow and Y. Yao, Interlayer-Expanded Molybdenum Disulfide Nanocomposites for Electrochemical Magnesium Storage, *Nano Lett.*, 2015, **15**, 2194–2202.

162 H. D. Yoo, Y. Liang, H. Dong, J. Lin, H. Wang, Y. Liu, L. Ma, T. Wu, Y. Li, Q. Ru, Y. Jing, Q. An, W. Zhou, J. Guo, J. Lu, S. T. Pantelides, X. Qian and Y. Yao, Fast kinetics of magnesium monochloride cations in interlayer-expanded titanium disulfide for magnesium rechargeable batteries, *Nat. Commun.*, 2017, **8**, 339.

163 F. Cui, M. Han, W. Zhou, C. Lai, Y. Chen, J. Su, J. Wang, H. Li and Y. Hu, Superlattice-Stabilized $WSe_2$ Cathode for Rechargeable Aluminum Batteries, *Small Methods*, 2022, **6**, 2201281.

164 Q. Liu, X. Weijun, Z. Wu, J. Huo, D. Liu, Q. Wang and S. Wang, The origin of the enhanced performance of nitrogen-doped $MoS_2$ in lithium ion batteries, *Nanotechnology*, 2016, **27**, 175402.

165 Y. Cai, H. Yang, J. Zhou, Z. Luo, G. Fang, S. Liu, A. Pan and S. Liang, Nitrogen doped hollow $MoS_2$/C nanospheres as anode for long-life sodium-ion batteries, *Chem. Eng. J.*, 2017, **327**, 522–529.

166 A. A. Kotsun, V. A. Alekseev, S. G. Stolyarova, A. A. Makarova, M. A. Grebenkina, A. P. Zubareva, A. V. Okotrub and L. G. Bulusheva, Effect of molybdenum disulfide doping with substitutional nitrogen and sulfur vacancies on lithium intercalation, *J. Alloys Compd.*, 2023, **947**, 169689.

167 Y.-C. Lin, D. O. Dumcenco, H.-P. Komsa, Y. Niimi, A. V. Krasheninnikov, Y.-S. Huang and K. Suenaga, Properties of Individual Dopant Atoms in Single-Layer $MoS_2$: Atomic Structure, Migration, and Enhanced Reactivity, *Adv. Mater.*, 2014, **26**, 2857–2861.

168 H. Shan, J. Qin, J. Wang, H. M. K. Sari, L. Lei, W. Xiao, W. Li, C. Xie, H. Yang, Y. Luo, G. Zhang and X. Li, Doping-Induced Electronic/Ionic Engineering to Optimize the Redox Kinetics for Potassium Storage: A Case Study of Ni-Doped $CoSe_2$, *Adv. Sci.*, 2022, **9**, 2200341.

169 P. Wen, H. Wang, X. Wang, H. Wang, Y. Bai and Z. Yang, Exploring the physicochemical role of Pd dopant in promoting Li-ion diffusion dynamics and storage performance of $NbS_2$ at the atomic scale, *Phys. Chem. Chem. Phys.*, 2022, **24**, 14877–14885.

170 S. Sovizi and R. Szoszkiewicz, Single atom doping in 2D layered $MoS_2$ from a periodic table perspective, *Surf. Sci. Rep.*, 2022, **77**, 100567.

171 X.-L. Fan, Y.-R. An and W.-J. Guo, Ferromagnetism in Transitional Metal-Doped $MoS_2$ Monolayer, *Nanoscale Res. Lett.*, 2016, **11**, 154.

172 Y. C. Cheng, Z. Y. Zhu, W. B. Mi, Z. B. Guo and U. Schwingenschlögl, Prediction of two-dimensional diluted magnetic semiconductors: Doped monolayer $MoS_2$ systems, *Phys. Rev. B: Condens. Matter Mater. Phys.*, 2013, **87**, 100401.

173 Q. Ding, W. Zheng, A. Zhao, Y. Zhao, K. Chen, X. Zhou, H. Zhang, Q. Li, X. Ai, H. Yang, Y. Fang and Y. Cao, W-Doping Induced Efficient Tunnel-to-Layered Structure Transformation of $Na_{0.44}Mn_{1-x}W_xO_2$: Phase Evolution, Sodium-Storage Properties, and Moisture Stability, *Adv. Energy Mater.*, 2023, **13**, 2203802.

 © 2024 The Author(s). Published by the Royal Society of Chemistry

Open Access Article. Published on 19 janvris 2024. Downloaded on 23.02.2025 18:44:43.
This article is licensed under a Creative Commons Attribution-NonCommercial 3.0 Unported Licence.

174 L. Xiao, F. Ji, J. Zhang, X. Chen and Y. Fang, Doping Regulation in Polyanionic Compounds for Advanced Sodium-Ion Batteries, *Small*, 2023, **19**, 2205732.

175 X. Zhao, P. Chen, C. Xia, T. Wang and X. Dai, Electronic and magnetic properties of n-type and p-doped $MoS_2$ monolayers, *RSC Adv.*, 2016, **6**, 16772–16778.

176 S. Lu, C. Li, Y. F. Zhao, Y. Y. Gong, L. Y. Niu and X. J. Liu, Tunable redox potential of nonmetal doped monolayer $MoS_2$: first principle calculations, *Appl. Surf. Sci.*, 2016, **384**, 360–367.

177 X. Sun and Z. Wang, Adsorption and diffusion of lithium on heteroatom-doped monolayer molybdenum disulfide, *Appl. Surf. Sci.*, 2018, **455**, 911–918.

178 R. Tian, A. Wu, G. Zhang, J. Liu, R. A. P. Camacho, W. Yu, S. Zhou, M. Yao and H. Huang, Adsorption and diffusion of alkali metals (Li, Na, and K) on heteroatom-doped monolayer titanium disulfide, *Dalton Trans.*, 2021, **50**, 7065–7077.

179 D. Wang, Y. Liu, X. Meng, Y. Wei, Y. Zhao, Q. Pang and G. Chen, Two-dimensional $VS_2$ monolayers as potential anode materials for lithium-ion batteries and beyond: first-principles calculations, *J. Mater. Chem. A*, 2017, **5**, 21370–21377.

180 F. Li, Y. Qu and M. Zhao, Germanium sulfide nanosheet: a universal anode material for alkali metal ion batteries, *J. Mater. Chem. A*, 2016, **4**, 8905–8912.

181 H. R. Jiang, W. Shyy, M. Liu, L. Wei, M. C. Wu and T. S. Zhao, Boron phosphide monolayer as a potential anode material for alkali metal-based batteries, *J. Mater. Chem. A*, 2017, **5**, 672–679.

182 S. Qin, W. Lei, D. Liu and Y. Chen, Advanced N-doped mesoporous molybdenum disulfide nanosheets and the enhanced lithium-ion storage performance, *J. Mater. Chem. A*, 2016, **4**, 1440–1445.

183 H. Xie, B. Chen, C. Liu, G. Wu, S. Sui, E.-Z. Liu, G. Zhou, C. He, W. Hu and N. Q. Zhao, Engineering the Interfacial Doping of 2D Heterostructures with Good Bidirectional Reaction Kinetics for Durably Reversible Sodium-Ion Batteries, *Energy Storage Mater.*, 2023, **60**, 102830.

184 J. Zhao, D. Xiao, Q. Wan, X. Wei, G. Tao, Y. Liu, Y. Xiang, K. Davey, Z. Liu, Z. Guo and Y. Song, Molybdenum Atom Engineered Vanadium Disulfide for Boosted High-Capacity Li-Ion Storage, *Small*, 2023, 2301738.

185 P. Wang, Z. Shen, Y. Xia, H. Wang, L. Zheng, W. Xi and S. Zhan, Atomic Insights for Optimum and Excess Doping in Photocatalysis: A Case Study of Few-Layer Cu-$ZnIn_2S_4$, *Adv. Funct. Mater.*, 2019, **29**, 1807013.

186 J. Zhang, C. Du, Z. Dai, W. Chen, Y. Zheng, B. Li, Y. Zong, X. Wang, J. Zhu and Q. Yan, $NbS_2$ Nanosheets with M/Se (M = Fe, Co, Ni) Codopants for $Li^+$ and $Na^+$ Storage, *ACS Nano*, 2017, **11**, 10599–10607.

187 T. Wang, C. Sun, M. Yang, G. Zhao, S. Wang, F. Ma, L. Zhang, Y. Shao, Y. Wu, B. Huang and X. Hao, Phase-transformation engineering in $MoS_2$ on carbon cloth as flexible binder-free anode for enhancing lithium storage, *J. Alloys Compd.*, 2017, **716**, 112–118.

188 Z. Sheng, P. Qi, Y. Lu, G. Liu, M. Chen, X. Gan, Y. Qin, K. Hao and Y. Tang, Nitrogen-Doped Metallic $MoS_2$ Derived from a Metal–Organic Framework for Aqueous Rechargeable Zinc-Ion Batteries, *ACS Appl. Mater. Interfaces*, 2021, **13**, 34495–34506.

189 F. Ersan, G. Gökoğlu and E. Aktürk, Adsorption and Diffusion of Lithium on Monolayer Transition Metal Dichalcogenides ($MoS_{2(1-x)}Se_{2x}$) Alloys, *J. Phys. Chem. C*, 2015, **119**, 28648–28653.

190 G. Barik and S. Pal, Monolayer Transition-Metal Dichalcogenide $Mo_{1-x}W_xS_2$ Alloys as Efficient Anode Materials for Lithium-Ion Batteries, *J. Phys. Chem. C*, 2018, **122**, 25837–25848.

191 G. Chaney, A. Ibrahim, F. Ersan, D. Çakır and C. Ataca, Comprehensive Study of Lithium Adsorption and Diffusion on Janus Mo/WXY (X, Y = S, Se, Te) Using First-Principles and Machine Learning Approaches, *ACS Appl. Mater. Interfaces*, 2021, **13**, 36388–36406.

192 J. Shi, H. Li, Y. Liu, Q. Lu and F. Gao, Molybdenum Sulfide Selenide Nanosheets Synergized with Nitrogen-Rich Carbon Frameworks toward High Performance and Stable Sodium Storage, *Adv. Mater. Interfaces*, 2022, **9**, 2102408.

193 Y. Yang, S. Wang, J. Zhang, H. Li, Z. Tang and X. Wang, Nanosheet-assembled $MoSe_2$ and S-doped $MoSe_{2-x}$ nanostructures for superior lithium storage properties and hydrogen evolution reactions, *Inorg. Chem. Front.*, 2015, **2**, 931–937.

194 G. Jia, D. Chao, N. H. Tiep, Z. Zhang and H. J. Fan, Intercalation Na-ion storage in two-dimensional $MoS_{2-x}Se_x$ and capacity enhancement by selenium substitution, *Energy Storage Mater.*, 2018, **14**, 136–142.

195 B. Liu, Y. Liu, X. Hu, G. Zhong, J. Li, J. Yuan and Z. Wen, N-Doped Carbon Modifying MoSSe Nanosheets on Hollow Cubic Carbon for High-Performance Anodes of Sodium-Based Dual-Ion Batteries, *Adv. Funct. Mater.*, 2021, **31**, 2101066.

196 K. Zhang, H. Zhang, C. Li and X. Ma, Vertically oriented $MoSe_{0.4}S_{1.6}$/N-doped C nanostructures directly grown on carbon nanotubes as high-performance anode for potassium-ion batteries, *J. Electroanal. Chem.*, 2022, **923**, 116846.

197 X. Yu, G. Zhao, C. Wu, H. Huang, C. Liu, X. Shen, M. Wang, X. Bai and N. Zhang, Constructing anion vacancy-rich MoSSe/G van der Waals heterostructures for high-performance Mg–Li hybrid-ion batteries, *J. Mater. Chem. A*, 2021, **9**, 23276–23285.

198 Y. Huang, Z. Wang, M. Guan, F. Wu and R. Chen, Toward Rapid-Charging Sodium-Ion Batteries using Hybrid-Phase Molybdenum Sulfide Selenide-Based Anodes, *Adv. Mater.*, 2020, **32**, 2003534.

199 A. Kutana, E. S. Penev and B. I. Yakobson, Engineering electronic properties of layered transition-metal dichalcogenide compounds through alloying, *Nanoscale*, 2014, **6**, 5820–5825.

200 C. Tan, W. Zhao, A. Chaturvedi, Z. Fei, Z. Zeng, J. Chen, Y. Huang, P. Ercius, Z. Luo, X. Qi, B. Chen, Z. Lai, B. Li, X. Zhang, J. Yang, Y. Zong, C. Jin, H. Zheng, C. Kloc and

Open Access Article. Published on 19 janvris 2024. Downloaded on 23.02.2025 18:44:43.
This article is licensed under a Creative Commons Attribution-NonCommercial 3.0 Unported Licence.

H. Zhang, Preparation of Single-Layer $MoS_{2x}Se_{2(1-x)}$ and $Mo_xW_{1-x}S_2$ Nanosheets with High-Concentration Metallic 1T Phase, *Small*, 2016, **12**, 1866–1874.

201 Q. Zhang, L. Wang, J. Wang, X. Yu, J. Ge, H. Zhang and B. Lu, Semimetallic vanadium molybdenum sulfide for high-performance battery electrodes, *J. Mater. Chem. A*, 2018, **6**, 9411–9419.

202 G. Cai, L. Peng, S. Ye, Y. Huang, G. Wang and X. Zhang, Defect-rich $MoS_{2(1-x)}Se_{2x}$ few-layer nanocomposites: a superior anode material for high-performance lithium-ion batteries, *J. Mater. Chem. A*, 2019, **7**, 9837–9843.

203 J. Xu, L. Dong, H. Tang and C. Li, Facile synthesis of $Mo_{0.91}W_{0.09}S_2$ ultrathin nanosheets/amorphous carbon composites for lithium-ion battery anode, *Ceram. Int.*, 2016, **42**, 7803–7809.

204 J. Dong, Y. Zhao, G. Ouyang and G. Yang, A perspective on optimizing photoelectric conversion process in 2D transition-metal dichalcogenides and related heterostructures, *Appl. Phys. Lett.*, 2022, **120**, 080501.

205 P. Tao, J. He, T. Shen, Y. Hao, J. Yan, Z. Huang, X. Xu, M. Li and Y. Chen, Nitrogen-Doped $MoS_2$ Foam for Fast Sodium Ion Storage, *Adv. Mater. Interfaces*, 2019, **6**, 1900460.

206 T. Wang, C. Sun, M. Yang, L. Zhang, Y. Shao, Y. Wu and X. Hao, Enhanced reversible lithium ion storage in stable 1T@2H $WS_2$ nanosheet arrays anchored on carbon fiber, *Electrochim. Acta*, 2018, **259**, 1–8.

 © 2024 The Author(s). Published by the Royal Society of Chemistry